Aus dem Physiologischen Institut der
Ludwig-Maximilians-Universität München
Vorstand Prof. Dr. M.Götz
Lehrstruhl für Physiologische Genomik

Kalziumdynamik in Körnerzellen
des Bulbus olfactorius
der Maus

Dissertation
zum Erwerb des Doktorgrades der Humanbiologie
an der Medizinischen Fakultät der
Ludwig-Maximilians-Universität zu München

vorgelegt von
Olga Stroh-Vasenev
aus Tomsk
2012

Mit Genehmigung der Medizinischen Fakultät
der Universität München

1. Berichterstatter:	Prof. Dr. Bernd Sutor
Mitberichterstatter:	Prof. Dr. Thomas Witt Priv.Doz. Dr. Eike Krause
Mitbetreuung durch den promovierten Mitarbeiter:	Dr. Veronica Egger

Dekan:
Prof. Dr. Dr.h.c. Maximilian Reiser, FACR, FRCR

Tag der mündlichen Prüfung: 18.09.2012

„Wäre das menschliche Gehirn so simpel, dass wir es erfassen könnten, wären wir so simpel, dass wir es nicht könnten.“

Immanuel Kant

Inhaltsverzeichnis

0   Zusammenfassung

Der häufigste neuronale Verbindungstyp im Riechkolben (Bulbus olfactorius) der Säuger ist die reziproke dendrodendritische Synapse zwischen den glutamatergen Mitralzellen (den Prinzipalneuronen des Bulbus) und den GABAergen Körnerzellen. Die dendritische Kalziumdynamik der axonlosen Körnerzellen ist aufgrund ihrer dendritischen Freisetzung von besonderem Interesse und zeichnet sich durch einen ungewöhnlich langsamen Verlauf aus. Zwei mögliche Ursachen dafür stehen im Zentrum dieser Dissertation: (1) Der unspezifische Kationenstrom I_{CAN}, der in Körnerzellen nach synaptisch evozierten Aktionspotenzialen beobachtet wird, und (2) die endogene Kalziumdynamik der Körnerzellen. Diese Phänomene wurden mittels Zwei-Photonen-Laser-Scan-Mikroskopie und simultaner Einzelzellableitung in akuten Hirnschnitten von adulten Mäusen untersucht.

In dieser Arbeit wurde die molekulare Identität von I_{CAN} als Kombination aus TRPC1 und TRPC4 (transient receptor potential classic) vermittels Tieren mit Deletionen der entsprechenden Gene aufgeklärt (Kollaboration mit Prof. Marc Freichel, Homburg). Im Vergleich zum Wildtyp fehlten in der TRPC1/4 Doppeldeletion I_{CAN} und der assoziierte langsame Ca^{2+}-Einstrom. Damit wurde erstmals eine synaptische Funktion von TRPC-Kanälen im Bulbus nachgewiesen. Weiterhin wurde ein bislang unbekannter Aktivierungsweg von TRPC-Kanälen entdeckt, nämlich über NMDA-Rezeptoren. Bezüglich der endogenen Kalziumdynamik wurde festgestellt, dass nicht etwa eine große Pufferkapazität dem langsamen Abbau von Ca^{2+}-Signalen zugrunde liegt, sondern vielmehr eine geringe Extrusionsrate. Damit sind beide Mechanismen – TRPC-Kanäle und endogene Kalziumdynamik – für den langsamen Verlauf von Ca^{2+}-Transienten in Körnerzellen mitverantwortlich.

0.1   Summary

The reciprocal dendrodendritic synapse between the principal glutamatergic mitral cells and the axonless GABAergic granule cells is the most abundant type of neuronal connection in the mammalian olfactory bulb. Because of the dendritic release the dendritic calcium dynamics of granule cells is of particular interest; it is characterized by a remarkably slow time course. This thesis centers on two possible mechanisms for the slow dynamics: (1) the non-specific cation current I_{CAN} that is activated in granule cells upon suprathreshold synaptic input and (2) the endogenous Ca^{2+} dynamics of granule cells. Here, the molecular identity of I_{CAN} was revealed as a combination of TRPC1- and TRPC4-channels (transient receptor potential, clas-

sic), using two-photon laser scan microscopy and simultaneous whole cell recordings. I_{CAN} and the associated slow Ca^{2+} entry were missing from the double deletion compared to wild type (cooperation with Prof. Marc Freichel, Homburg), demonstrating for the first time an involvement of TRPC channels in synaptic processing in the olfactory bulb. Moreover, a hitherto unknown pathway of TRPC activation was discovered – via NMDA receptors. With respect to the endogenous Ca^{2+} buffering, it was shown that slow extrusion is responsible for the slow decay of Ca^{2+}- signals, not an unusually high buffer capacity. Thus both mechanisms, TRPC channels and endogenous Ca^{2+} dynamics, contribute to the slow time course of granule cell Ca^{2+} signals.

1   Einleitung

1.1   Synaptische Verschaltung im Bulbus olfactorius

Eine der grundlegenden Aufgaben des Gehirns ist die Verarbeitung von sensorischen Informationen. Der Geruchssinn, obschon beim Menschen im Laufe der Evolution zurückentwickelt, ist überlebenswichtig für viele Säugetiere. Insbesondere viele Nagetierarten sind aufgrund ihres Lebensstils im Dunkeln auf olfaktorische Informationen aus ihrer Umwelt zur Orientierung, Nahrungs- und Partnersuche angewiesen. Die Geruchsinformation wird von den chemischen Sinnesrezeptoren der Nase aufgenommen, durchläuft komplexe Verarbeitungsprozesse im Riechkolben (*Bulbus olfactorius*) und wird an den olfaktorischen Kortex weitergeleitet (Abb. 1A). Die Prinzipalneuronen des Bulbus olfactorius, also die Mitral- und Büschelzellen, werden von den olfaktorischen Rezeptorneuronen direkt innerviert und projizieren zum olfaktorischen Cortex. Zwar bilden sie keine direkten synaptischen Kontakte miteinander, dafür sind sie jedoch disynaptisch gekoppelt über Synapsen mit den inhibitorischen axonlosen Körnerzellen. Dieses weitgespannte Netzwerk bewerkstelligt den Hauptanteil der Geruchsverarbeitung im Bulbus.

Diese Verschaltung erfolgt vor allem über reziproke Synapsen der lateralen Mitralzelldendriten mit den Körnerzelldendriten (Abb. 1A,B). Auf der Seite der Körnerzelle beinhalten die Synapsen prä- und postsynaptische Elemente gemeinsam in großen Dornfortsätzen (Spines). Glutamatfreisetzung aus den Mitralzelldendriten erregt die Körnerzelldendriten über AMPA- und NMDA-Rezeptoren. Der Kationeneinstrom in die Körnerzelle bewirkt eine Depolarisation der Membran und damit ein exzitatorisches postsynaptisches Potential (EPSP). Wenn die Depolarisation stark genug ist, wird ein Aktionspotenzial (AP) ausgelöst, das sich im Körnerzelldendriten ausbreitet, es kommt zum Einstrom von Ca^{2+} über spannungsabhängige Ca^{2+}-Kanäle und andere Kanäle. GABA wird aus den reziproken Spines freigesetzt und inhibiert die Mitralzellen über $GABA_A$-Rezeptoren. Bei dieser Freisetzung von GABA aus dem Körnerzell-Spine gibt es zwei Besonderheiten. Zum einen kann sie bereits unterschwellig erfolgen, zum anderen gibt es eine deutliche asynchrone Komponente.
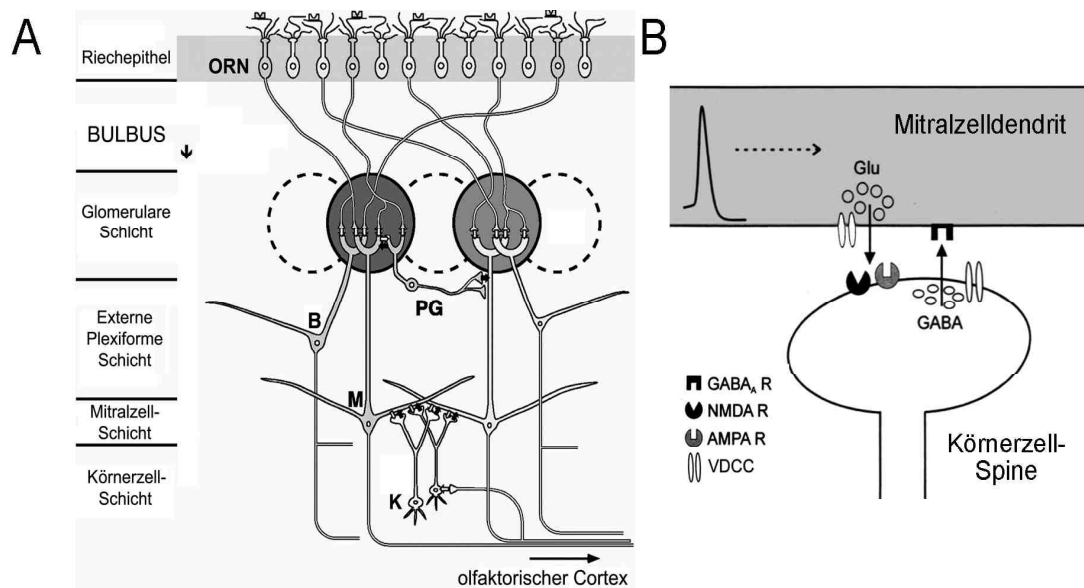
Abb. 1: ***A*** Schema der Schichten und der synaptischen Organisation des Bulbus olfactorius der Säugetiere. Zwei glomeruläre Module repräsentieren zwei unterschiedliche Typen der Geruchsrezeptoren. ORN: olfaktorisches Rezeptorneuron, M: Mitralzelle, B: Büschelzelle, PG: Periglomerularneurone, K: Körnerzelle. ⇨ erregende Synapse, ➔ hemmende Synapse. Modifiziert nach *Mori et al. 1999*.
B Die reziproke dendrodendritische Mitralzell-Körnerzell-Synapse. Schematische Ansicht der reziproken dendrodendritischen Synapse. VDCC: Spannungsabhängige Kalziumkanäle (*voltage-dependent calcium channels*). Modifiziert nach *Isaacson & Strowbridge 1998*.

Obwohl die Körnerzellen des Bulbus olfactorius auf den ersten Blick ungewöhnlich erscheinen mögen, ist ihre Physiologie verwandt mit der anderer neuronaler Zelltypen, die auch dendritische Freisetzung als Merkmal aufweisen, z.B. thalamische GABAerge Interneurone und retinale amakrine Zellen (*Shepherd & Greer 2004*). Da in der olfaktorischen Signalleitung die thalamische Verschaltung fehlt, könnten die Ähnlichkeiten zwischen thalamischen Interneuronen und Körnerzellen auf einer noch nicht erschlossenen analogen Funktion bei der Signalverarbeitung beruhen (*Kay & Sherman 2007*). Folglich sind Körnerzellen von allgemeinem Interesse für die sensorische Signalverarbeitung.

1.2   Dendritische synaptische Kalziumsignale in Körnerzellen

Es gibt mehrere Arten von Kalziumsignalen in Körnerzellen, die durch Aktivierung von Mitralzellen hervorgerufen werden können:

(1) Eine lokale Aktivierung von nur einem einzelnen Spine führt zu einer Selbsthemmung (rekurrente Inhibition) der aktivierenden Mitralzelle. Dabei aktiviert eine Mitralzelle einen Spine einer Körnerzelle, der als Antwort GABA auf dieselbe Mitralzelle

freisetzt. Dies kann ohne eine globale Depolarisation der Körnerzelle und folglich ohne deren AP geschehen (*Jahr & Nicoll 1980, 1982, Isaacson & Strowbridge 1998, Chen et al. 2000, Halabisky et al. 2000*). In der Tat führt eine solche Aktivierung eines einzelnen Körnerzell-Spines zu einem substantiellen lokalen Kalziumeintritt, der im Wesentlichen durch NMDA-Rezeptoren, spannungsgesteuerte Ca^{2+}-Kanäle und Freisetzung aus internen Speichern vermittelt wird (*Egger et al. 2005*).

(2) Durch die simultane Aktivierung mehrerer Spines kann ein sogenanntes niederschwelliges Ca^{2+}-AP (*low threshold spike*, LTS), ausgelöst werden, das auf der Öffnung spannungs-abhängiger Kalziumkanäle vom T-Typ beruht. Ein LTS breitet sich in der gesamten Körnerzelle aus und verursacht damit einen globalen Ca^{2+}-Einstrom (*Egger et al. 2003, 2005, Pinato & Midtgaard 2003*). Der LTS könnte erklären, warum laterale Inhibition von Mitralzellen (d.h. von Zellen, die nicht direkt an der Aktivierung der Körnerzelle beteiligt waren), auch in Gegenwart von Tetrodotoxin beobachtet werden kann (*Isaacson & Strowbridge 1998*).

(3) Mit einem Na^{+}-AP der Körnerzelle ist ebenfalls ein globaler Ca^{2+}-Einstrom assoziiert, der etwas schneller im Anstieg und grösser in der Amplitude ausfällt als der LTS-vermittelte Einstrom (*Egger et al. 2003, 2005*). Es sind wieder alle reziproken Synapsen der aktivierten Körnerzelle betroffen. Somit kann ebenfalls laterale Inhibition vermittelt werden. Die durch diese Zellen vermittelte Geruchsinformation wird dadurch abgeschwächt.

1.3   Langsamer Zeitverlauf der Körnerzell-vermittelten Inhibition

Unter Spannungsklemmenbedingungen werden in Mitralzellen nach kurzen Depolarisationen synchrone und asynchrone inhibitorische Ströme beobachtet (*Jahr & Nicoll 1982, Isaacson & Strowbridge 1998, Schoppa & Westbrook 1998*). Der Zeitverlauf der dendrodendritischen Selbsthemmung ist damit vergleichsweise langsam ($\tau \approx 500$ ms). Der zugrundeliegende Mechanismus ist nur teilweise verstanden, jedoch mit großer Wahrscheinlichkeit auf Seiten der Körnerzelldendriten lokalisiert, da erregende postsynaptische Potenziale (EPSPs) in Körnerzellen nach Mitralzellstimulation vorwiegend mit kurzen Latenzen auftreten.

Folgende intrinsische Mechanismen werden diskutiert: *Schoppa et al. (1999)* erklärt die asynchrone Freisetzung durch eine Verzögerung des Körnerzell-APs aufgrund des stark ausgeprägten Kaliumstroms I_A. Allerdings sind Körnerzell-APs für die Freisetzung von GABA nicht unbedingt erforderlich (siehe 1.2). Eine langsame Ca^{2+}-Freisetzung aus internen Speichern der Körnerzelle ist ebenfalls nicht beteiligt (*Chen et al. 2000*). Weiterhin wäre es denkbar, dass langsamer synaptischer Ca^{2+}-Einstrom durch NMDA-Rezeptoren asynchrone

Freisetzung ermöglicht. Aufgrund der Schwierigkeit, geeignete pharmakologische Experimente an der reziproken Synapse durchzuführen, die nicht die synaptische Freisetzung aus dem Mitralzelldendriten beeinträchtigen, bleibt diese Möglichkeit ein Gegenstand der Diskussion. Die AMPA-Rezeptoren der Körnerzellen tragen auf Grund ihrer niedrigen Ca^{2+}-Permeabilität (*Jardemark et al.1997*) nicht direkt zu den Ca^{2+}-Transienten bei.

In der ersten vorliegenden Publikation wird ein weiterer Mechanismus aufgeklärt, der zu einem verlängerten Ca^{2+}-Einstrom in die gesamte Körnerzelle führt (siehe unten). Wir konnten nachweisen, dass dieser verlängerte Einstrom an der Vermittlung asynchroner Freisetzung beteiligt ist.

Eine weitere mögliche Ursache für die asynchrone Freisetzung aus Körnerzellen könnte eine besonders hohe endogene Ca^{2+}-Pufferkapazität κ_E sein, ähnlich wie bei Purkinje-Neuronen des Kleinhirns (*Fierro & Llano 1996*). Diese Vermutung wird durch die ungewöhnlich langsamen AP-vermittelten dendritischen Ca^{2+}-Signale nahegelegt, die mit Ca^{2+}-sensitiven Fluoreszenzfarbstoffen beobachtet wurden (*Egger et al. 2003, 2005, Pinato and Midtgaard 2005, Zelles et al. 2006*). Bei physiologischer Temperatur und gleichem Farbstoff sowie Farbstoffkonzentration zeigen die Körnerzell-Ca^{2+}-Signale mit einer Zerfallszeitkonstanten von ~ 400 ms gegenüber ~100 ms in neokortikalen Pyramidenzellen der Schicht V oder ~ 200 ms in CA1 Pyramidalzellen des Hippokampus einen vergleichsweise langsamen Zeitverlauf (*Egger et al. 2003, Markram et al. 1995; Sabatini et al. 2002*).

Die Bestimmung der endogenen Pufferkapazität κ_E und der Ca^{2+}-Extrusionsrate ist daher ebenfalls ein wichtiger Gegenstand der hier vorliegenden Untersuchungen und steht im Zentrum der zweiten vorliegenden Publikation.

1.4   Synaptische Körnerzell-Aktionspotenziale

Sofern die synaptische Aktivierung der Körnerzellen zu einem Na^+-AP führt, ist sie meist mit einer langanhaltenden Depolarisation (*longlasting depolarization*, LLD) verbunden. Diese LLD konnte nach durch Mitralzellstimulation ausgelösten APs in Körnerzellen des olfaktorischen Bulbus des Frosches (*Hall & Delaney 2002*) und der Ratte (*Egger 2008*) beobachtet werden. Ein durch somatische Strominjektion evoziertes Na^+-AP sowie das niederschwellige Ca^{2+}-AP weisen diese LLD nicht auf. Mittels Ca^{2+}-Imaging wurde nachgewiesen, dass die LLD mit einem zusätzlichen globalen Ca^{2+}-Einstrom assoziiert ist (*Egger 2008*). Der zugrundeliegende Plateaustrom erfordert die Aktivierung von NMDA-Rezeptoren und korrespondiert mit der unspezifischen Kationenleitfähigkeit I_{CAN}, die bereits

beim Frosch beschrieben wurde *(Hall & Delaney 2002)*. Der globale Ca^{2+}-Einstrom kommt durch die Aktivierung von T-Typ-Ca^{2+}-Kanälen während der LLD zustande. Die schematische Abfolge dieser Ereignisse ist in Abb.2 zu sehen. Aufgrund des langsamen Ca^{2+}-Einstroms könnte die LLD eine Rolle bei der asynchronen Mitralzellhemmung spielen.
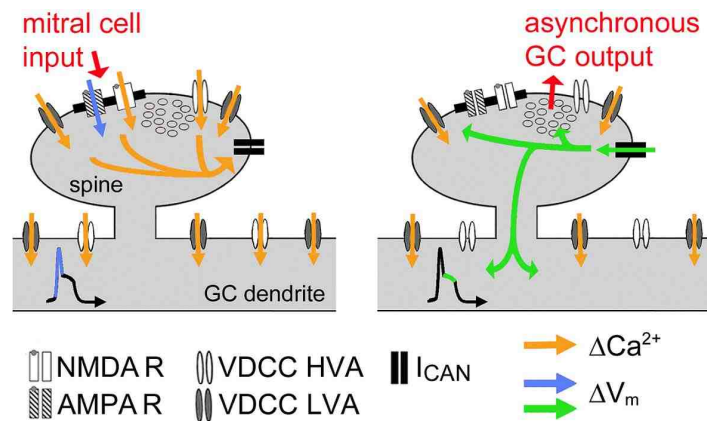

Abb. 2: Schema der Aktivierungsabfolge während des synaptischen Körnerzell-APs. Links: Die synaptische Aktivierung eines Spines in Verbindung mit einem Körnerzell-Aktionspotenzial resultiert in einem Ca^{2+}-Einstrom in den Spine über NMDA-Rezeptoren (NMDAR) und spannungsabhängige Ca^{2+}-Kanäle (*voltage dependent calcium channel*, VDCC). Der gemeinsamen NMDAR- und VDCC-Aktivität folgt die Aktivierung des unspezifischen Kationenstroms I_{CAN}, möglicherweise über Ca^{2+}-Einstrom. Rechtes Schema: Die Aktivierung des I_{CAN} ihrerseits führt zu einer LLD, welche die T-Typ-Kanäle (*low voltage activated*, LVA VDCC) in Aktion hält und dadurch einen globalen Ca^{2+}-Einstrom während des Plateaus ermöglicht. (aus *Egger 2008*).

Die molekulare Identität des unspezifischen Kationenstroms I_{CAN} ist der Hauptgegenstand der vorliegenden ersten Publikation. Die Abhängigkeit des Plateaustroms von einem synaptischen Ca^{2+}-Einstrom und die lange Dauer legen eine Verbindung zur Familie der TRPC-Kanäle nahe.

1.5 Rolle der TRP-Kanäle beim neuronalen Kalziumeintritt

Ca^{2+}-induzierte neuronale Ca^{2+}-Signale werden zunehmend mit der TRP-Kanal-Superfamilie in Verbindung gebracht. Die Familie ist in mehrere Kanalgruppen aufgeteilt, wobei TRPC die kanonischen oder klassischen Kanäle sind, die auch im Zentralnervensystem anzutreffen sind (*Clapham 2003, Montell 2005*). Alle Mitglieder dieser Superfamilie sind Kationenkanäle. Die meisten von ihnen sind am Ca^{2+}-Einstrom im Rahmen intrazellulärer Signalkaskaden beteiligt. Die Art ihrer Aktivierung unterscheidet sich jedoch von Gruppe zu Gruppe, ja teilweise von Kanal zu Kanal: mechanisch, temperaturabhängig, osmotisch, chemisch über intra- oder

extrazelluläre Agonisten inklusive metabotroper Signalkaskaden oder über den Füllstand der internen Ca^{2+}-Speicher (z. B. *Harteneck et al. 2000, Clapham et al. 2001, Mortell 2001*).
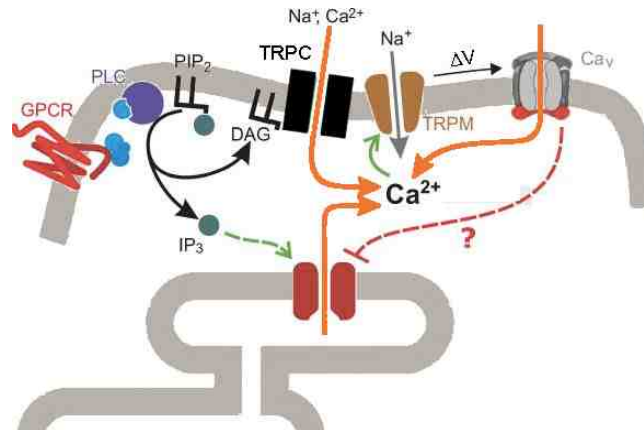

Abb. 3: Einbindung der TRPC-Kanal-Proteine in intrazelluläre Signalkaskaden zur Regulierung des Membranpotenzials und damit der spannungabhängigen Ionenkanäle und der zytosolischen Ca^{2+}-Konzentration. GPCR: G-Protein gekoppelter (*coupled*) Rezeptor, PLC: Phospholipase C, PIP_2: Phosphatidylinositol-4,5-biphosphat, IP_3: Inositol-1,4,5-triphosphat, DAG: Diazylglyzerol, Ca_V: Spannungsabhängiger Ca-Kanal, $\Delta\psi$: Änderung des Membranpotenzials (Modifiziert nach Freichel et al. 2005).

Die TRPC-Kanäle werden seit ihrer Identifizierung am Ende des letzten Jahrhunderts als einer der wichtigsten Mechanismen für den durch Neurotransmitter, Hormone oder Wachstumsfaktoren aktivierten Ca^{2+}-Einstrom in allen Zellarten angesehen *(z.B. Freichel et al. 2004, 2005, Vazquez 2004, Berridge 1998, Ambudkar et al. 2007)* Die Zellkommunikation über Ca^{2+}-Signale speziell in Neuronen erfolgt durch elektrische und chemische synaptische Übertragung, bei der typischerweise eine metabotrope Aktivierung der TRPC-Kanäle erfolgt (Abb. 3; *Braet et al. 2004*). Histochemische Untersuchungen zeigten ein weit verbreitetes Vorkommen der TRPC-Kanäle im Maushirn *(Mori et al. 1998, Strubing et al. 2003, Zechel et al. 2007)*, gehäuft unter anderem im Hippocampus, Bulbus olfactorius, Thalamus und Cerebellum.

Die TRPC-Gruppe besteht aus sieben Mitgliedern, TRPC1-7. Mehrere Studien belegen, dass die TRPC-Kanäle nicht nur als homomere, sondern auch als homomultimere und heteromultimere Strukturen auftreten *(Strubing et al. 2001, 2003, Hofmann et al. 2002, Goel et al. 2002)*.

Studien an transgenen Mauslinien mit Deletionen einzelner *TRPC*-Gene erlauben die Dissoziation unterschiedlicher Funktionen der einzelnen Kanäle (*Freichel et al. 2005*). Unter anderem spielen TRPC-Kanäle eine wichtige Rolle in neuronalen Prozessen. Z.B. beeinflusst TRPC5 speziell im Hippocampus das axonale Wachstum (*Freichel et al. 2004, Montell 2005*).

Das *TRPC2*-Gen ist beim Menschen zurückentwickelt, spielt dagegen bei den Nagetieren eine sehr wichtige Rolle in der Pheromonwahrnehmung über das vomeronasale Organ und damit bei der sexuellen Kommunikation und Aggressionsregulierung bei männlichen Nagetieren (*Stowers et al. 2002, Leypold 2002*). Interessanterweise wird die dendritische Freisetzung von GABA aus thalamischen Interneuronen von TRPC4 mitbestimmt (*Munsch et al. 2003, Pape et al. 2004*).

1.6 Ziele der vorliegenden Arbeit

1.6.1 Aufklärung der molekularen Identität von I_{CAN} (Stroh et al. 2012)

Die hier dargestellten Eigenschaften der TRPC-Kanäle zusammen mit den oben geschilderten Beobachtungen des langsamen Ca^{2+}-Einstroms auf Grund der Aktivierung von I_{CAN} in Körnerzellen führten zur Arbeitshypothese, dass es sich bei I_{CAN} um einen TRPC-Kanal-vermittelten Strom handelt und TRPC-Kanäle somit an der synaptischen Verarbeitung in den Mitralzell-Körnerzell reziproken Synapsen beteiligt sein könnten. Dazu war es zunächst erforderlich, nachzuweisen, dass die in der juvenilen Ratte beobachteten Phänomene tatsächlich auch in der Maus vorliegen.

1.6.2 Endogene Pufferung von Körnerzell-Ca^{2+}-Signalen (Egger und Stroh, 2009)

Da eine hohe Pufferkapazität für Ca^{2+} ähnlich wie I_{CAN} zu asynchroner Freisetzung aus den Spines der Körnerzellen beitragen könnte, wurden Pufferkapazität und Extrusionsrate aus der Messung absoluter Ca^{2+}-Konzentrationen in Ruhe und am Maximum von somatischen AP und saturierenden AP-Folgen mit unterschiedlichen Farbstoffkonzentrationen bestimmt (*Maravall et al. 2000*).

1.7 Eigener Beitrag

Während die vorangegangenen Arbeiten zur Körnerzell-Ca^{2+}-Dynamik an akuten Hirnschnitten juveniler Ratten durchgeführt wurden (*Egger et al. 2003, 2005; Egger, 2008*), habe ich für die Durchführung dieser Arbeit elektrophysiologische Einzelzell-Ableitungen an Körnerzellen in Hirnschnitten der adulten Maus im Labor etabliert. Die synaptischen Mitralzell-Eingänge wurden mit glomerulärer Stimulation erregt; hier habe ich bei der Optimierung unseres Eigenbau-Stimulators mitgewirkt. Die Technik der mit Zwei-Photonen-Ca^{2+}-Imaging gekoppelten Einzelzellableitung wurde von mir erfolgreich im Rahmen beider Projekte angewandt; die Datenanalyse wurde weitgehend eigenständig durchgeführt. Hinsichtlich der in den Veröffentlichungen enthaltenen Daten habe ich zu der Arbeit *Stroh et al. (2012)* den Großteil der experimentellen Daten beigetragen, nur an den

Mitralzellexperimenten (Fig. 6) und Teilen der pharmakologischen Experimente (Fig. 2CD) sowie der Immunhistochemie habe ich keinerlei Anteil. Weiterhin habe ich auch unpublizierte Messungen an Hirnschnitten von Mäusen mit Deletion des *TRPC6*-Gens, mit Doppeldeletion von *TRPC6* und *TRPC4* und mit Tripeldeletion von *TRPC6, TRPC4* und *TRPC1* durchgeführt. Zur Arbeit *Egger und Stroh (2009)* habe ich im Wesentlichen die Messungen in der Maus (Fig. 3, z.T. Fig. 2) und einige Messungen mit Fluo-5F in der Ratte beigetragen.

1.8   Referenzen

Ambudkar IS, Ong HL, Liu X, Bandyopadhyay B, Cheng KT. (2007) *TRPC1: the link between functionally distinct store-operated calcium channels*. Cell Calcium, 42: 213-223.

Berridge MJ. (1998) *Neuronal calcium signalling*. Neuron, 21(1): 13-26.

Braet K, Cabooter L, Paemeleire K, Leybaert L. (2004) *Calcium signal communication in the central nervous system*. Biology of the Cell, 96: 79-91.

Clapham DE. (2003) *TRP channels as cellular sensors*. Nature, 426: 517-524.

Egger V, Svoboda K, Mainen ZF. (2003) *Mechanisms of lateral inhibition in the olfactory bulb: efficiency and modulation of spike-evoked calcium influx into granule cells*. Journal of Neuroscience, 23: 7551–7558.

Egger V, Svoboda K, Mainen ZF. (2005) *Dendrodendritic synaptic signals in olfactory bulb granule cells: local spine boost and global low-threshold spike.* Journal of Neuroscience, 25: 3521–3530.

Egger V. (2008) *Synaptic sodium spikes trigger long-lasting depolarizations and slow calcium entry in rat olfactory bulb granule cells.* European Journal of Neuroscience, 27(8): 2066-75.

Fierro L, Llano I. (1996) *High endogenous calcium buffering in Purkinje cells from rat cerebellar slices*. Journal of Physiology, 496: 617-25.

Freichel M, Vennekens R, Olausson J, Hoffmann M, Müller C, Stolz S, Scheunemann J, Weissgerber P, Flockerzi V. (2004) *Functional role of TRPC proteins in vivo: lessons from TRPC-deficient mouse models*. Biochemical and Biophysical Research Communications, 322: 1352-1358.

Freichel M, Vennekens R, Olausson J, Stolz S, Philipp SE, Weissgerber P, Flockerzi V. (2005) *Functional role of TRPC proteins in native systems: implications from knockout and knock-down studies*. Journal of Physiology, 567(1): 59-66.

Goel M, Sinkins WG, Schilling WP. (2002) *Selective association of TRPC channel subunits in rat brain synaptosomes*. Journal of Biological Chemistry, 277(50):48303-10.

Halabisky B, Friedman D, Radojicic M, Strowbridge BW. (2000) *Calcium influx through NMDA receptors directly evokes GABA release in olfactory bulb granule cells*. Journal of Neuroscience, 20: 5124-5134.

Hall BJ, Delaney KR. (2002) *Contribution of a calcium-activated non-specific conductance to NMDA receptor-mediated synaptic potentials in granule cells of the frog olfactory bulb*. Journal of Physiology, 543(3): 819-834.

Harteneck C, Plant TD, Schultz G. (2000*) From worm to man: three subfamilies of TRP channels*. Trends in Neuroscience, 23(4): 159-166.

Hofmann T, Schäfer M, Schultz G, Gudermann T. (2002) *Subunit composition of mammalian transient receptor potential channels in living cells*. PNAS, 99(11): 7461-66.

Isaacson JS, Strowbridge BW. (1998) *Olfactory reciprocal synapses: dendritic signaling in the CNS*. Neuron, 20: 749-761 (1998)

Jahr CE, Nicoll RA. (1980) *Dendrodendritic inhibition: demonstration with intracellular recording*. Science, 207: 1473-1475.

Jahr CE, Nicoll RA. (1982) *An intracellular analysis of dendrodendritic inhibition in the turtle in vitro olfactory bulb*. Journal of Physiology, 326: 213-234.

Jardemark K, Nilsson M, Muyderman H, Jacobson I. (1997) *Ca2+ ion permeability properties of (R,S) alpha-amino-3-hydroxy-5-methyl-4-isoxazolepropionate (AMPA) receptors in isolated interneurons from the olfactory bulb of the rat*. Journal of Neurophysiology, 77: 702-708.

Kay LM, Sherman SM. (2007) *An argument for an olfactory thalamus.* Trends in Neuroscience, 30(2): 47-53.

Leypold BG, Yu CR, Leinders-Zufall T, Kim MM, Zufall F, Axel R. (2002) *Altered sexual and social behaviours in trp2 mutant mice*. PNAS, 99(9):6376-81.

Markram H, Helm PJ, Sakmann B. (1995) *Dendritic calcium transients evoked by single back-propagating action potentials in rat neocortical pyramidal neurons*. Journal of Physiology, 485: 1–20.

Montell C. (2005) *The TRP superfamily of cation channels*. Science's STKE: signal transduction knowledge environment, 2005(272): Re3.

Mori Y, Takada N, Okada T, Wakamori M, Imoto K, Wanifuchi H, Oka H, Oba A, Ikenaka K, Kurosaki T. (1998) *Differentail distribution of TRP Ca^{2+} channel isoforms in mouse brain*. NeuroReport, 9: 597-515.

Mori K, Nagao H, Yoshihara Y. (1999) *The olfactory bulb: coding and processing of odor molecule information.* Science, 286: 711-715.

Munsch T, Freichel M, Flockerzi V, Pape H-C. (2003) *Contribution of transient receptor potential channels to the control of GABA release from dendrites*. PNAS, 100(26): 16065-16070.

Pape HC, Munsch T & Budde T. (2004) *Novel vistas of calcium-mediated signalling in the thalamus*. Pflügers Archiv, 448: 131–138.

Pinato G, Midtgaard J. (2003) *Regulation of granule cell excitability by a low-threshold calcium spike in turtle olfactory bulb.* Journal of Neurophysiology, 90(5): 3341-3351.

Sabatini BL, Oertner TG, Svoboda K. (2002) *The life cycle of Ca(2+) ions in dendritic spines*. Neuron, 33: 439–452.

Schoppa NE, Kinzie JM, Sahara Y, Segerson TP, Westbrook GL. (1998) *Dendrodendritic inhibition in the olfactory bulb is driven by NMDA receptors*. Journal of Neuroscience, 18: 6790-6802.

Schoppa NE, Westbrook GL. (1999) *Regulation of synaptic timing in the olfactory bulb by an A-type potassium current.* Nature Neuroscience, 2: 1106-1113.

Shepherd GM, Greer CA. (2004) *Olfactory bulb*. In: Shepherd GM, editor. The synaptic organization of the brain. 5th edition, New York: Oxford University Press. p.165-216.
Chen WR, Xiong W, Shepherd GM. (2000) *Analysis of relations between NMDA receptors and GABA release at olfactory bulb reciprocal synapses*. Neuron, 25: 625-633.

Stowers L, Holy TE, Meister M, Dulac C, Koentgens G. (2002) *Loss of sex discrimination and male-male aggression in mice deficient for TRP2*. Science, 295(5559): 1493-500.

Strübing C, Krapivinsky G, Krapivinsky L, Clapham DE. (2001) *TRPC1 and TRPC5 form a novel cation channel in mammalian brain*. Neuron, 29: 645-655.

Strübing C, Krapivinsky G, Krapivinsky L, Clapham DE. (2003) *Formation of novel TRPC channels by complex subunit interactions in embryonic brain*. Journal of Biological Chemistry, 278: 39014-39019.

Vazquez G, Wedel BJ, Aziz O, Trebak M, Putney JW Jr. (2004) *The mammalian TRPC cation channels*. Biochimica et Biophysica Acta, 1742(1-3): 21-36.

Zechel S, Werner S, Bohlen U, Halbach O. (2007) *Distribution of TRPC4 in developing and adult murine brain*. Cell and Tissue Research, 328: 651-656.

Zelles T, Boyd JD, Hardy AB, Delaney KR. (2006) *Branch-specific Ca2+ influx from Na+-dependent dendritic spikes in olfactory granule cells*. Journal of Neuroscience, 26: 30–40.

2 Ergebnisse

2.1 NMDA-receptor dependent synaptic activation of TRPC channels in olfactory bulb granule cells

Abbreviated title: NMDA-R dependent TRPC-mediated synaptic currents

Olga Stroh[1], Marc Freichel[2], Oliver Kretz[3], Lutz Birnbaumer[4], Jana Hartmann[5], Veronica Egger[1,6]

1. Physiological Institute, LMU, München, Germany

2. Institute of Pharmacology and Toxicology, Universität des Saarlandes, Homburg, Germany

3. Department of Anatomy and Cell Biology, University of Freiburg, Freiburg, Germany

4. NIEHS, Research Triangle Park North Carolina, USA

5. Institute for Neuroscience, TUM, München, Germany

6. Department of Biology II, Division of Neurobiology, LMU, München, Germany

Corresponding author:

Veronica Egger

Department of Biology II, Division of Neurobiology, LMU Grosshadernerstr. 2

D-82152 Martinsried, Germany

Email: V.Egger@lmu.de

Phone: + 49 89 2180 74338

Fax: + 49 89 2180 74304

Abstract

TRPC channels are widely expressed throughout the nervous system including the olfactory bulb where their function is largely unknown. Here we describe their contribution to central synaptic processing at the reciprocal mitral and tufted cell - granule cell microcircuit, the most abundant synapse of the mammalian olfactory bulb. Suprathreshold activation of the synapse causes sodium action potentials in mouse granule cells and a subsequent long-lasting depolarization (LLD) linked to a global dendritic postsynaptic calcium signal recorded with two-photon laser scanning microscopy. These signals are not observed after action potentials evoked by current injection in the same cells. The LLD persists in the presence of group I metabotropic glutamate receptor antagonists but is entirely absent from granule cells deficient for the NMDA receptor subunit NR1. Moreover, both depolarization and Ca^{2+} rise are sensitive to the blockade of NMDA receptors. The LLD and the accompanying Ca^{2+} rise are also absent in granule cells from mice deficient for both TRPC channel subtypes 1 and 4, whereas the deletion of either TRPC1 or TRPC4 results in only a partial reduction of the LLD. Recordings from mitral cells in the absence of both subunits reveal a reduction of asynchronous neurotransmitter release from the granule cells during recurrent inhibition. We conclude that TRPC1 and TRPC4 can be activated downstream of NMDA receptor activation and contribute to slow synaptic transmission in the olfactory bulb, including the calcium dynamics required for asynchronous release from the granule cell spine.

Introduction

The most abundant type of synaptic connection in the vertebrate olfactory bulb is the reciprocal dendrodendritic synapse between the mitral/tufted cells (MTCs) and granule cells (GCs) where glutamate is released from the MTC dendrite onto the GC spine that in turn can release GABA. Sufficient excitation of GC dendrites results in the spread of inhibition to other MTCs. Thus the synapse can mediate both recurrent and lateral inhibition of MTCs (reviewed in (Shepherd and Greer, 2004)). Both types of inhibition show a prominent asynchronous component that lasts up to several 100 ms ((Jahr and Nicoll, 1980); (Isaacson and Strowbridge, 1998)) and is probably located within the GC compartment of the reciprocal microcircuit (Chen et al., 2000), contained by large spines also known as gemmules. Possible mechanisms include an I_A current that delays GC spiking ((Schoppa and Westbrook, 1999); (Kapoor and Urban, 2006)), and sluggish extrusion of Ca^{2+} from the gemmule (Egger and Stroh, 2009).

In addition, we have suggested that the non-selective cation current I_{CAN} first identified in frog GCs (Hall and Delaney, 2002) may also promote asynchronous release (Egger, 2008). In both frog and rat GCs, this plateau current and the associated long-lasting depolarization (LLD) are supported by NMDA-receptor (NMDAR) activation and blocked by both flufenamic acid and increased intracellular Ca^{2+} buffering. In the olfactory bulb, LLDs are present in many neuronal classes, e.g. an NMDAR-independent form in mitral cells (Carlson et al. 2000). In GCs, a slow global extra Ca^{2+} entry was directly correlated to the duration of the LLD and mediated by the persistent activation of T-type voltage-dependent Ca^{2+} currents (VDCCs; Egger, 2008).

Several of these properties resemble that of slow synaptic currents mediated by TRPC (Transient Receptor Potential, Canonical) channels that have been described recently elsewhere in the CNS ((Amaral and Pozzo-Miller, 2007); (Fowler et al., 2007); (Hartmann et al., 2008); (Clapham, 2007); (Becker et al., 2009)). The seven TRPC channels, one of six subfamilies of the TRP cation channel superfamily, are expressed in many cell types (Reviews e.g. (Moran et al., 2004); (Birnbaumer, 2009)). In the nervous system, TRPCs were initially identified in sensory nerve endings and later found also in axons and dendrites of central neurons. Functionally, TRPCs have been mostly implicated in sensory transduction and neurite outgrowth and development with a role in synaptic transmission emerging only recently. For example, while TRPC2 has been identified to play a crucial role in pheromone detection in the vomeronasal system (reviewed in (Zufall et al., 2005)), there is no functional data on TRPC action in the main olfactory bulb so far.

Here we tested the hypothesis that a TRPC channel is the molecular correlate of I_{CAN} in GCs, using electrophysiological recordings and two-photon laser scanning microscopy of local Ca^{2+} signals in GCs of mice deficient for different subtypes of TRPC proteins. We demonstrate a direct involvement of TRPC channels in synaptic excitation in higher sensory processing, and provide evidence for a novel, NMDAR-mediated mechanism of activation of TRPCs that also affects neurotransmitter release from GC dendrites.

Materials and Methods

Animals, slice preparation and electrophysiology

TRPC1/TRPC4 double-knockout (*TRPC1/4* DKO) mice were generated by breeding *TRPC1-/-* (Dietrich et al., 2007) and *TRPC4-/-* mice (Freichel et al., 2001). To generate *TRPC1/TRPC4/TRPC5* triple-knockout mice (used as controls for immunohistochemistry) the DKO mice were bred with mice in which exon 4 of the *TRPC5* gene was deleted (Xue et al., 2011). All *TRPC*-deficient mice were on a mixed 129SvJ genetic background. The mice with the GC-specific NR1-knockout were the same as the ones used in (Abraham et al., 2010) (cf. their Methods for the generation of the mice, injection of the virus and the visualization of infected GCs using two-photon imaging). Sagittal olfactory bulb brain slices (thickness 250 μm) were prepared of WT and mutant mice of either sex (PND 16-213, WT Bl6 and 129SvJ strain), in accordance with the EC Council directives for animal care. For the influence of age on the physiological readout see Results. All experiments were performed at room temperature (~ 21° C). For all current-clamp experiments in GCs the intracellular solution contained [mM]: 130 K-methylsulfate, 10 HEPES, 4 $MgCl_2$, 4 Na_2ATP, 0.4 NaGTP, 10 NaPhosphocreatine, 2 ascorbate, at pH 7.2, and in addition 100 μM of the calcium-sensitive dye OGB-1 (Invitrogen, Carlsbad, CA, USA) for imaging experiments. The extracellular ACSF was bubbled with carbogen and contained [mM]: 125 NaCl, 26 $NaHCO_3$, 1.25 NaH_2PO_4, 20 Glucose, 2.5 KCl, 1 $MgCl_2$ and 2 $CaCl_2$. Pharmacological agents used were D-APV (25 μM; Sigma), YM289189 and MPEP (10 μM and 40 μM; Tocris). For voltage clamp experiments in mitral cells, the internal solution contained [mM]: 125 Cs-methylsulfate, 10 HEPES, 10 TEA, 4 $MgCl_2$, 2.5 Na_2ATP, 0.4 NaGTP, 10

NaPhosphocreatine, 2 ascorbate, 10 mM QX-314 at pH 7.2. The ACSF was the same as above, except for the omission of $MgCl_2$.

Cells were recorded from in whole-cell mode with an EPC-9 amplifier (Heka, Lambrecht, Germany).

Activation of the MTC input was achieved via glomerular stimulation (cf. Egger 2008) using an STG-1004 stimulator (MultiChannelSystems, Reutlingen, Germany). To ensure sufficient connectivity for suprathreshold stimulation, most patched GCs were located close to the mitral cell layer, i.e. superficially, and thus were likely to be connected to both mitral and tufted cells (Orona et al. 1983). Synaptic APs in GCs were evoked by glomerular stimulation (glAPs), artificial APs (sAP) were evoked by brief somatic current injections (1 ms, 1000 pA). The average resting potential was at $V_m = -79 \pm 4$ mV (n = 17). GCs were generally held at a potential of -70 to -80 mV; cells that required more than 50 pA of holding current were not accepted.

For mitral cell recordings in voltage clamp we used pipettes sized 4-6 MΩ and achieved series resistances R_s below 20 MΩ. R_s was monitored during the experiments. Dendrodendritic recurrent inihibition (DDI) was elicited by depolarizing mitral cells from -70 mV to 0 mV for 20 ms. To prevent rundown, DDI was measured only every 60 - 120 s and analysed after its amplitude stabilized (usually about 20 min after break in). A subset of GCs both in WT and *TRPC1/4* DKO were also filled with biocytin and processsed and reconstructed using Neurolucida (Microbrightfield, USA), as described previously (Lubke et al., 2000).

18

Two-photon imaging

Imaging was performed on an Fluoview 300 system (Olympus), with two-photon excitation at 800 nm provided by a Ti:Sapphire solid-state laser system (Mai Tai, Spectraphysics, CA, USA).

Immunohistochemistry

Young adult WT and *TRPC1/4/5* triple knockout mice were anesthetized and transcardially perfused with 4% PFA in 0.1 M PB. Animals assigned to fine structure analysis were perfused with a fixative containing 4% PFA and 0.05% glutaraldehyde in 0.1 M PB. The olfactory bulbs were removed, cut coronally (section thickness 50 µm) on a vibratome and the sections were stored in PB. For immunofluorescence labeling with rabbit-anti-TRPC1, rabbit-anti-TRPC4 or rabbit-anti-TRPC5, respectively, sections were washed in 0.1 M PB and incubated in a blocking solution (5 % normal goat serum, 2 % bovine serum albumin, 0.1 % TritonX in PB) for unspecific protein binding sites for 60 min. Sections were then incubated with the primary antibodies (final concentration 0.5 µg/µl in blocking solution; overnight at 4°C). Then, sections were washed in PB and incubated with secondary goat anti-rabbit antibody coupled to cy3 for 45 min (1:600; Dianova, Germany) at room temperature. Finally, sections were washed in PB, counter stained using DAPI (30 s; Hoechst, Germany), washed again in PB, and mounted for image analysis.

For electron microscopy, sections of the olfactory bulb sections were washed in PBS and cryoprotected in a solution containing 25% sucrose and 10% glycerol in 50 mM

PBS. The sections were freeze-thawed and incubated in blocking solution containing 5% NGS in 0.1 M PB for 1 h, followed by incubation with primary antibodies (final concentration 2μg/μl, for 24 h at 4°C). After washing in phosphate buffer, the sections were incubated with biotinylated goat anti-rabbit secondary antibody (1:250, Vector Laboratories Inc.) for 4 h at room temperature, washed, and finally incubated for 1 h at room temperature with ABC solution (Vector Elite Kit, Vector Laboratories Inc.). Visualization of the antibody binding was performed using peroxidase reaction with diaminobenzidine (DAB) as the substrate. To exclude unspecific staining due to the secondary antibody, we performed negative controls using the same staining procedure except primary antibody incubation. After the sections were treated with OsO_4, they were stained with uranyl acetate, dehydrated, and flat-embedded in epoxy resin (Durcupan ACM, Fluka; Sigma-Aldrich). Ultrathin sections were cut and analyzed with a Philips CM100 electron microscope.

Data analysis

Two-photon imaging data were analyzed as described previously (Egger, 2008). Changes in calcium were measured in terms of $\Delta F/F$ (Egger et al., 2005). Throughout the paper, $\tau_{1/2}$ denotes half durations from the peak amplitude of changes in $\Delta F/F$ or V_m onward, that were in the case of V_m measured between the onset of the LLD/ADP right after the sodium spike and half of its maximum amplitude. Both LLD amplitude and $\tau_{1/2}$ are often analysed relative to the ADP following sAPs in order to eliminate variabilities that arise from the non-synaptic component of the LLD, i.e. the ADP: The smaller the

20

ratio, the stronger the synaptic contribution. The averaged dendrodendritic inhibition recorded in mitral cells was analysed with respect to its $\tau_{1/2}$ and total charge after the stimulus artefact.

To assess statistical significance levels, the nonparametric Wilcoxon matched-pairs signed-ranks test was applied for comparing paired data sets, e.g. parameters of the sAP and glAP in the same cells, while the non-parametric Mann-Whitney test was used to compare unpaired data, e.g. the ADP half duration in young versus adult animals. The entire set of data from WT, *TRPC1* KO, *TRPC4* KO and *TRPC1/4* KO animals presented in Figure 3D was compared using the Kruskal-Wallis test; differences between individual data pairs were evaluated with the Mann-Whitney test followed by the appropriate Bonferroni-Holm correction. All averages are given $\pm$ S.D.

Results

Synaptic spikes mediate long-lasting depolarization and correlated Ca^{2+} entry in mouse GCs

To verify the presence of the synaptic plateau current I_{CAN} in mouse GCs we applied glomerular stimulation of MTC apical dendritic tufts ((Schoppa et al., 1998); Figure 1A; 500-800 μA pulses, 100 μs duration) in acute brain slices (PND 17-132) while recording in whole-cell current clamp mode from GCs. This stimulation evoked excitatory postsynaptic potentials in GCs. Upon suprathreshold stimulation strength, the synaptic depolarization resulted in "glomerular action potentials" (glAPs). Similar to our previous findings in rat, these glAPs were frequently followed by a long-lasting depolarization (LLD) as shown in Figure 1C (mean amplitude above resting potential 17.7 ± 6.4 mV, mean half duration $\tau_{1/2}$ 176 ± 175 ms, n = 49 GCs). The LLD was significantly larger and longer-lasting than the afterdepolarization (ADP) following current-evoked "somatic action potentials" (sAPs) in the same cells (by somatic injection of a 1000 pA step for 1 ms), with a mean sAP-ADP amplitude above resting potential 11.1 ± 4.7 mV and a mean half duration $\tau_{1/2}$ 42 ± 22 ms ($P < 0.001$ for both; Figure 1D). On average, the LLD lasted also considerably longer than the glomerular EPSP recorded just below the glomerular AP threshold in the same cell ($\tau_{1/2}$ 166 ± 174 ms vs 88 ± 58 ms, n = 39, $P < 0.001$). Thus the LLD is not just a barrage of EPSPs due to MTC-GC network activity; its generation most likely requires both synaptic input and a Na^+ AP.

The occurrence of the LLD did not depend on the age of the animals: Upon averaging the LLD and ADP $\tau_{1/2}$ and amplitude data in three age groups of WT mice - young (P16-P22; n = 32), juvenile (P32-P42, n = 6) and adult (P66-P139, n = 7) - we found that although both amplitude and duration of the plateau decreased slightly with age, I_{CAN} was activated in all three groups (all significance levels LLD vs ADP for both amplitudes and $\tau_{1/2}$: $P < 0.005$). The

average LLD $\tau_{1/2}$ was always significantly longer than the average EPSP $\tau_{1/2}$ just below threshold (P66-P139: P < 0.01).

To verify that the LLD is also correlated to global Ca^{2+} entry, we used two-photon laser scan imaging to analyze Ca^{2+} entry into GCs at high spatial resolution. We found that the LLD is accompanied by extra, slow Ca^{2+} entry both in the dendrite and the large reciprocal GC spines similar to our previous findings in rat (Egger, 2008). Figure 1C shows $\Delta F/F$ transients in a spine and its parent dendrite of a mouse GC. $(\Delta F/F)_{glAP}$ was found to decay significantly more slowly than $(\Delta F/F)_{sAP}$ in the same locations ($\tau_{1/2}$ 1200 ± 800 ms vs 750 ± 460 ms, n = 40 spines in 27 cells, P < 0.001; Figure 1D). The amplitudes of $(\Delta F/F)_{glAP}$ were as large or larger than of $(\Delta F/F)_{sAP}$ (39 ± 15 % vs 33 ± 14%, amplitude ratio glAP/sAP 1.21 ± 0.28, P < 0.001). For both data sets, there were no significant differences between dendrites and spines, so in Figure 1D all data are pooled (n = 51 locations).

LLD requires GC NMDARs but not mGluRs

In frog and rat GCs the activation of the plateau current I_{CAN} was found to require a cytosolic rise in $[Ca^{2+}]$; synaptically evoked plateau currents were sensitive to NMDAR blockade (Hall and Delaney, 2002) (Egger, 2008). Like in other species, mouse NMDARs already participate in basal MTC-GC synaptic transmission under near-resting conditions ((Laaris et al., 2007); (Abraham et al., 2010)).

As shown in Figure 2A,B, application of 25 μM D-APV markedly reduced the LLD half duration and amplitude (235 ± 236 ms vs 92 ± 44 ms; 20.8 ± 8.1 mV vs 15.6 ± 6.8 mV, P < 0.002 for both; n = 15 cells). As to the $[Ca^{2+}]$ transients, APV made $(\Delta F/F)_{glAP}$ decay as quickly as $(\Delta F/F)_{sAP}$ and have the same amplitude (($\tau_{1/2}$ ratio glAP/sAP control 2.26 ± 1.10 vs APV 0.92 ± 0.08; n = 6, P < 0.025; amplitude ratio control 1.34 ± 0.29 vs APV 1.06 ± 0.12; n

= 7, P < 0.025). There was no effect of APV on $(\Delta F/F)_{sAP}$ (mean amplitude control 28 ± 8 % vs APV 26 ± 10%).

Given that APV might exert presynaptic effects on MTC NMDA autoreceptors ((Isaacson, 1999); (Salin et al., 2001)) or affect the efficiency of glomerular stimulation (but see (Egger et al., 2005); (Egger, 2008)), we also tested for the existence of the LLD in GCs that were deficient for the essential NMDAR subunit NR1. The GC-specific deletion was achieved via viral expression of Cre recombinase in GCs of conditional GluN1^{2lox} animals (Abraham et al., 2010). In none of the GCs tested was there any indication of a plateau current. The mean glAP/sAP ratio was 0.97 ± 0.10 for the amplitude and 1.00 ± 0.14 for $\tau_{1/2}$ of the afterdepolarization (Figure 2C), while the absolute sAP ADP amplitudes and $\tau_{1/2}$ were not significantly different from the WT values given above (NR1 KO: ADP amplitude 13.0 ± 5.6 mV, ADP_$\tau_{1/2}$ 29 ± 19 ms; n = 5 cells). Because MTCs were not infected, this experiment allows to exclude any unspecific effects of NMDAR blockade on synapses other than those of GCs. Thus the activation of NMDARs located in GCs is essential for the generation of the LLD and the concomitant Ca^{2+} entry.

Slow depolarizing currents such as I_{CAN} have been associated with activation of G-protein coupled receptors, in particular group I metabotropic receptors (e.g. (Congar et al., 1997), (Pace et al., 2007)). So far, GCs are known to prominently express either mGluR5 or mGluR1, depending on their depth within the GCL, and accordingly the application of group I agonists was found to increase GC excitability (reviewed in (Dong et al., 2009)). To test for a role of group I mGluRs, we first recorded control responses, then co-applied 10 μM of the mGluR1-antagonist YM289189 and 40 μM of the mGluR5-antagonist MPEP and recorded GC responses after at least 10 min of wash-in. This procedure has been reported to block mGluRs in acute brain slices (e.g. (Fukunaga et al., 2007), (Zheng and Raman, 2011)). Figure 2D shows that blockade of group I mGluRs did not decrease the LLD $\tau_{1/2}$ and amplitude (297

± 287 ms vs 336 ± 315 ms; 22.2 ± 5.6 mV vs 21.6 ± 5.3 mV; n = 5 cells; compare to APV results above). Thus group I mGluRs do not play an essential role in the generation of the LLD.

TRPC channels mediate the LLD

Another possible candidate for the mechanism underlying the plateau current is the activation of TRPC channels, because members of this channel family cause depolarization via their non-selective cation conductance and have been associated previously with plateau-like currents (Birnbaumer, 2009). TRPC4 is the most abundant TRPC in the olfactory bulb ((Lein et al., 2007); (Zechel et al., 2007)). We confirmed the presence of TRPC4 protein in the GC layer (GCL; Figure 3Aa,b) and the external plexiform layer (EPL) of the mouse OB, also at the ultrastructural level (Figure 4A-D) with anti-TRPC4 antibodies. Then we tested for the existence of an LLD in GCs of *TRPC4*-deficient mice (*TRPC4*-/-; (Freichel et al., 2001)). To render the graphical depiction more compact, the following data are presented in Figure 3B-D as ratios of sAP to glAP afterdepolarization values. In the absence of TRPC4 the plateau current following the synaptic AP was reduced and, accordingly, the sAP/glAP-ADP $\tau_{1/2}$ ratio was significantly larger than in the WT (0.64 ± 0.16, n = 14 vs 0.38 ± 0.23, n = 49; P < 0.001 for both), while the ADP ratios, the absolute mean ADP amplitude and $\tau_{1/2}$ were similar in *TRPC4*-/- and WT (P > 0.05 for all). Thus, NMDAR-dependent plateau currents were significantly reduced but not completely absent in *TRPC4*-/- mice (compared to the NR1 deletion described above).

TRPC4 belongs to a subgroup of TRPC subunits with two other members – TRPC1 and TRPC5. All three readily associate with each other forming heteromeric channels ((Goel et al., 2002); (Strubing et al., 2001); (Hofmann et al., 2002)). Further immunohistochemistry with anti-TRPC1 antibodies confirmed the presence of TRPC1 protein in the GCL (Figure

3Ac,d) and the EPL of the mouse OB, also at the ultrastructural level (Figure 4E-H). Expression of TRPC5 in GCs was not observed (data not shown). Thus, we hypothesized that the remaining LLD in the *TRPC4-/-* mice is carried by TRPC1. Indeed, in mice deficient for both *TRPC1* and *TRPC4* (*TRPC1/4* double knockout, DKO) the plateau currents were almost completely absent (Figure 3B-D). Here, both the amplitude and $\tau_{1/2}$ ratios were significantly different from the WT (n = 21 vs n = 49; P < 0.001 for both), whereas the absolute sAP-ADP amplitude and $\tau_{1/2}$ were unaltered in the *TRPC1/4* DKO animals compared to WT mice (P > 0.05 for both). The remaining small difference between sAP- and glAP-afterdepolarizations is explained by the EPSP underlying the glAP: the $\tau_{1/2}$ values of the EPSP just below threshold and the glAP-afterdepolarization were similar in the *TRPC1/4* DKO (71 ± 54 ms vs 69 ± 38 ms, n = 21); accordingly the $\tau_{1/2}$ ratio of sAP-ADP/EPSP is the same as for sAP-ADP/glAP-ADP (Figure 3D). Moreover, the EPSP $\tau_{1/2}$ values were not significantly different between *TRPC1/4* DKO and WT (P = 0.40), reinforcing the notion that EPSPs alone do not suffice to generate the LLD.

Our finding that both TRPC4 and TRPC1 contribute to the long-lasting synaptic signals in OB GCs was corroborated by results obtained in *TRPC1-/-* mice (n = 7 GCs; Figure 3B-D). In summary, the deletion of either *TRPC1* or *TRPC4* caused significantly smaller effects on the plateau current $\tau_{1/2}$ ratios than the deletion of both genes (*TRPC1-/-* vs DKO P < 0.05 and *TRPC4 -/-* vs DKO P < 0.02; statistical significances for ADP ratio comparisons between different mouse lines evaluated by Kruskal-Wallis test followed by pairwise Mann-Whitney test with appropriate Bonferrroni-Holm correction).

We then tested whether the extra Ca^{2+} entry associated with the plateau was also abolished in the *TRPC1/4* DKO animals, using TPLSM. Indeed, the amplitudes and half durations of $(\Delta F/F)_{glAP}$ and $(\Delta F/F)_{sAP}$ were equal in the DKO GCs (36 ± 13 % vs 35 ± 14 % and

580 ± 380 ms vs 590 ± 340 ms; n = 28 locations in 11 cells; both P > 0.1; Figure 5B, C). Accordingly, both the amplitude and $\tau_{1/2}$ ratios of $(\Delta F/F)_{sAP}$ to $(\Delta F/F)_{gIAP}$ were significantly larger than in the WT (P < 0.001), and not significantly different from 1 (0.97 ± 0.08 and 1.04 ± 0.20, P > 0.25, single sample T-test). Thus, NMDAR-dependent extra Ca^{2+} entry evoked by suprathreshold synaptic input is absent in *TRPC1/4* DKO mice.

Deletion of TRPC1 and TRPC4 does not reduce excitability

The general deletion of both *TRPC1* and *TRPC4* could indirectly impede the LLD generation by detrimental effects on the neuronal excitability of MTCs and GCs (Cvetkovic-Lopes et al., 2010). The aforementioned immunohistochemistry with anti-TRPC1 and anti-TRPC4 antibodies yielded no evidence for the presence of any of the two proteins in olfactory receptor neuron axons. Mitral cells expressed both TRPC1 and TRPC4 while tufted cells showed only expression of TRPC1 (data not shown). Thus we investigated effects of the *TRPC1/4* double deletion on synaptic transmission between MTCs and GCs and also GC excitability *per se*.

As to the shape of the GC Na^+ AP in WT and DKO animals, both amplitude and width did not show any significant differences (for absolute data and P levels of this section see Table 1). The frequency of APs in response to a depolarizing current pulse at 50 pA and 800 ms duration did also not differ significantly between the two populations. The frequency was evaluated for cells responding at this current amplitude; the fraction of silent cells was 0.35 in the WT and 0.39 in the DKO. The input resistance of the two groups was similar. Also, the average extracellular stimulation threshold for the generation of synaptic APs was equal, and as stated above, the EPSP $\tau_{1/2}$ just below AP threshold was the same for both. We also tested for possible effects of the *TRPC1/4* DKO on GC morphology (see Methods), but did not

observe any major changes with respect to the total length of the apical dendrite as well as to the number of its branchpoints.

While more subtle effects cannot be excluded, these data speak against a major alteration of GC excitability and MTC to GC synaptic transmission in the absence of TRPC1/4.

TRPCs promote slow feedback inhibition of mitral/tufted cells

The MTC-GC microcircuit can provide recurrent inhibition of MTCs via dendritic release of GABA from the reciprocal GC spine. This release occurs in part asynchronously (see Introduction). A role for TRPC4 in dendritic release has been previously demonstrated in thalamic GABAergic neurons (Munsch et al., 2003). Because in GCs TRPC activation via MTC input results in slow extra Ca^{2+} entry, we hypothesized that the slow TRPC-mediated plateau current facilitates recurrent dendrodendritic inhibition of MTCs.

In order to measure recurrent inhibition we voltage-clamped mitral cells and applied brief depolarizing pulses that are known to activate the microcircuit and cause recurrent GABA release ((Jahr and Nicoll, 1980); (Isaacson and Strowbridge, 1998)). To reduce voltage escape, QX-314 was included in the pipette solution, and NMDAR activation was facilitated by omitting Mg^{2+} from the ACSF ((Isaacson and Strowbridge, 1998; Schoppa et al., 1998); (Chen et al., 2000); (Halabisky et al., 2000)). Figure 6 illustrates that the decay kinetics of the resulting barrage of IPSCs was significantly faster in the *TRPC1/4* DKO than in the WT mice ($\tau_{1/2}$ DKO 70 ± 30 ms, n = 8 cells vs WT 280 ± 140 ms, n = 7 cells, P < 0.005). The amplitudes across these experiments were highly variable, probably owing to the differing connectivity in acute slices, but not significantly different between the two populations. There was no correlation between the amplitudes and the half durations (WT r = -0.27; DKO r = -0.31). However, the integrals of the responses were larger in the WT (143 ± 115 nA ms) than

28

in the DKO (43 ± 27 nA ms; $P < 0.025$). Thus we conclude that TRPC-mediated Ca^{2+} entry contributes to dendritic GABA release from the GC spine and fosters in particular late/asynchronous recurrent inhibition.

Discussion

TRPC activation cascade

We have demonstrated that TRPC1 and TRPC4 are required for a synaptic, I_{CAN}-mediated plateau current at the MTC–GC synapse. This conclusion is based on the absence of plateau currents at this synapse in the combined deletion of *TRPC1* and *TRPC4*, while individual deletion of either *TRPC1* or *TRPC4* is accompanied by partial reductions in the plateau current amplitude and duration. We find that synaptic activation of TRPC1/4 is achieved via NMDA receptor-mediated signalling.

Although TRPC channels are regulated by intracellular Ca^{2+}/calmodulin (reviewed in (Zhu, 2005)), so far their activation was found to critically depend on G_q-protein coupled receptors in other examples of neuronal TRPC action: In cerebellar Purkinje cells, an mGluR1-dependent slow EPSP has been shown to be mediated by TRPC3 (Hartmann et al., 2008). Activation of a TRPC channel downstream of synaptic activation of mGluR1 has been suggested also for hippocampal oriens/alveus interneurons (Topolnik et al., 2006) and CA1 pyramidal cells (El-Hassar et al., 2011). In the amygdala, synaptic responses downstream of mGluR1 and the cholecystokinin$_2$ receptor are significantly reduced in *TRPC5-/-* mice (Riccio et al., 2009). In a heterologous expression system mGluR1 is able to couple to TRPC1 (Kim et al., 2003).

The dependence of TRPC channel opening on the activation of an ionotropic glutamate receptor has not been described before. Current views hold that TRPC channels are activated by phospholipase C (PLC)-coupled metabotropic receptors (e.g. (Soboloff et al., 2007)). Consistent with that, a group I mGluR-specific agonist-evoked inward current was recorded in OB GCs (Heinbockel et al., 2007). In addition, muscarinic acetylcholine receptors at the MTC–GC synapse were found to be coupled to an FFA-sensitive I_{CAN} in GCs ((Ghatpande and Gelperin, 2009); (Pressler et al., 2007)), similarly to neurons in the entorhinal cortex (Zhang

et al., 2011). However, the lack of an effect of group I mGluR blockade on the GC LLD, the blockade of the LLD by APV, the triggering of the LLD by single stimulation - versus the repetitive stimulation that is often required to activate mGluRs - and the fact that ryanodine receptors but not IP_3 receptors contribute to basal synaptic Ca^{2+} signaling in GC spines (Egger et al., 2005) rule out an essential involvement of metabotropic receptors in the type of synaptic response that we investigate here.

An mGluR-independent PLC activation following glutamate binding to NMDARs was observed in hippocampal neurons ((Horne and Dell'Acqua, 2007); (Codazzi et al., 2006)). This effect is mediated by PLCδ isoforms (Codazzi et al., 2006) that are not controlled by G_q but directly activated by Ca^{2+} (Allen et al., 1997). We have shown previously that NMDARs contribute a significant fraction to postsynaptic calcium signals at the reciprocal MTC-GC synapse (Egger et al., 2005). Ca^{2+} influx through the NMDAR channel is of crucial importance for the LLD in OB granule cells ((Egger, 2008); (Hall and Delaney, 2002)), and PLCδ isoforms are expressed in the GC layer (Lein et al., 2007). It remains to be elucidated whether NMDAR-mediated $\Delta[Ca^{2+}]_i$ acts onto the TRPCs via PLCδ or whether the signaling pathway involves other steps. For TRPC3 in cerebellar Purkinje cells, a PLC-independent gating mechanism relies on the small GTP-binding protein Rho and subsequent phospholipase D activation (Glitsch, 2010). TRPC channels are known to be redundantly activated and appear to be located at a point of intersection of diverse signaling pathways (reviewed in (Hartmann et al., 2011)). Moreover, TRPC channels in neurons are part of multi-protein postsynaptic signaling complexes that also contain neurotransmitter receptors, including the NMDAR (reviewed in (Ambudkar et al., 2006)). E.g. the cholesterol-binding protein caveolin-1 can scaffold NMDARs and Src protein kinases (Head et al., 2008) and attach TRPC subunits to the plasma membrane ((Lockwich et al., 2000); (Brazer et al., 2003)). Src protein kinases, in turn, have been shown to activate both TRPC1 (Gervasio et al., 2008) and TRPC4 (Odell et al., 2005).

31

At the MTC-GC synapse, the absence of synaptic plateau currents in the *NR1*-KO GCs argues against an activation of TRPCs via ryanodine receptors.

Since the coincidence of NMDAR activation and a Na^+ spike is required to activate the TRPCs, we suggest that the relevant signal cascade is triggered by the elevation of $[Ca^{2+}]_i$ via NMDARs only if this elevation is enhanced by the membrane depolarization provided by the Na^+ spike, either via additional relief of the Mg^{2+}-block or via activation of VDCCs, just as in classical coincidence detection mechanisms that play a role in synaptic plasticity (e.g. (Blair et al., 2001)).

Finally, it has been debated whether TRPC1 on its own can be a pore-forming subunit (reviewed e.g. in (Wu et al., 2010)). We still find a plateau current (albeit reduced) in the absence of TRPC4, that is most likely mediated by TRPC1. Thus apparently TRPC1 homomultimers can conduct currents in olfactory bulb GCs.

Functional roles of TRPC activation

TRPC activation results in a global Ca^{2+} entry in dendrites and spines of the GC that is due to T–type Ca^{2+} channel activation caused by the depolarizing plateau current (Egger, 2008). This prolonged Ca^{2+} entry persists during the plateau current and thus may contribute to delayed dendritic release of GABA. Indeed, we show that recurrent inhibition is faster and involves less charge transfer in *TRPC1/4* DKO animals. We propose that TRPC1 and TRPC4 are key players in the regulation of slow dendritic GABA release from GCs, similar to the role of TRPC4 in thalamic interneurons (Munsch et al., 2003). Obviously, however, TRPCs are not the only effectors of slow output from this system, since asynchronous release also occurs in the presence of TTX (e.g. (Isaacson and Strowbridge, 1998)), is not fully blocked in the DKO and there are also other mechanisms providing prolonged Ca^{2+} entry such as delayed GC spik-

ing ((Schoppa and Westbrook, 1999); (Kapoor and Urban, 2006)) and sluggish extrusion of Ca^{2+} from the GC dendrite (Egger and Stroh, 2009).

How does TRPC1/4 action then shape odor processing in the olfactory bulb? An implicit answer to this question is provided by the study of Abraham et al. (2010), where a GC-specific deletion of NR1 was achieved in approx. 40% of all GCs of the OB (GluN1$^{\Delta GCL}$). In these cells the activation of TRPC1/4 is also blocked, as shown above by the lack of the LLD for glomerularly evoked action potentials. Accordingly, recurrent inhibition following trains of APs is also reduced in GluN1$^{\Delta GCL}$ mice *in vitro*. Behavioural tests showed that in GluN1$^{\Delta GCL}$ mice learning and memory are not affected although the discrimination of highly similar odorants takes significantly more time than in WT mice. Thus, TRPC action could also be related to fine odor discrimination; it remains to be elucidated what aspect of the above observations is due to other actions of the NMDAR apart from downstream TRPC-mediated effects.

However, since a major part of TRPC action appears to happen on the slow temporal time scale and odor discrimination has been shown to occur rather fast we would also expect other roles of TRPC to emerge. For example, TRPC action may couple to the prominent slow, respiration-coupled oscillations intrinsic to the olfactory bulb (e.g. (Macrides and Chorover, 1972)), possibly via their interaction with T-type VDCCs (T-channels). We have already proposed that GC T-channels are periodically inactivated by slow olfactory bulb oscillations and thus GC output is likely to be also periodically modulated (Egger et al., 2003). The TRPC-channel mediated long-lasting depolarizations can activate T-channels and thus produce global Ca^{2+} entry (Egger, 2008) and participate in driving slow bulbar oscillations, but may also contribute to the periodic inactivation of T-channels in the course of these persistent depolarizations.

In addition to its importance for recurrent inhibition, the TRPC-mediated mechanism of LLD demonstrated here might play a role in lateral inhibition of neighboring MTCs, again by giving rise to global extra Ca^{2+} entry. Lateral inhibition will usually co-occur with TRPC activation because the latter requires a GC Na^+ spike. The spike will propagate along the GC dendrite and cause substantial Ca^{2+} entry at other reciprocal spines ((Egger et al., 2003); (Zelles et al., 2006)) that is enhanced by the TRPC-mediated extra global Ca^{2+} entry. Lateral inhibition *per se* does not necessarily require a Na^+ spike (Isaacson and Strowbridge, 1998) but may also be triggered by a Ca^{2+} spike in GCs (Pinato and Midtgaard, 2003; Egger et al., 2005) that is probably not capable of activating TRPCs. Nevertheless, the efficiency and duration of lateral inhibition following a GC AP are very likely to be enhanced by TRPC1/4 action. Thus, even though Ca^{2+} entry via NMDARs may not couple directly to recurrent GABA release (Isaacson, 2001), NMDAR activation can contribute to recurrent and lateral inhibition via the TRPC-mediated pathway.

Finally, we have shown that in GCs Na^+ spikes evoked by current injection are *not* equivalent to Na^+ spikes evoked by synaptic mitral and tufted cell input because only the latter are capable of TRPC activation and produce a different spatio-temporal pattern of postsynaptic Ca^{2+} entry. This finding may contribute to the recent debate on the validity of paradigms used to determine spike-timing dependent plasticity (Lisman and Spruston, 2010).

References

Abraham NM, Egger V, Shimshek DR, Renden R, Fukunaga I, Sprengel R, Seeburg PH, Klugmann M, Margrie TW, Schaefer AT, Kuner T (2010) Synaptic inhibition in the olfactory bulb accelerates odor discrimination in mice. Neuron 65:399-411.

Allen V, Swigart P, Cheung R, Cockcroft S, Katan M (1997) Regulation of inositol lipid-specific phospholipase cdelta by changes in Ca2+ ion concentrations. Biochem J 327 (Pt 2):545-552.

Amaral MD, Pozzo-Miller L (2007) TRPC3 channels are necessary for brain-derived neurotrophic factor to activate a nonselective cationic current and to induce dendritic spine formation. J Neurosci 27:5179-5189.

Ambudkar IS, Bandyopadhyay BC, Liu X, Lockwich TP, Paria B, Ong HL (2006) Functional organization of TRPC-Ca2+ channels and regulation of calcium microdomains. Cell Calcium 40:495-504.

Becker EB, Oliver PL, Glitsch MD, Banks GT, Achilli F, Hardy A, Nolan PM, Fisher EM, Davies KE (2009) A point mutation in TRPC3 causes abnormal Purkinje cell development and cerebellar ataxia in moonwalker mice. Proc Natl Acad Sci U S A 106:6706-6711.

Birnbaumer L (2009) The TRPC class of ion channels: a critical review of their roles in slow, sustained increases in intracellular Ca(2+) concentrations. Annu Rev Pharmacol Toxicol 49:395-426.

Blair HT, Schafe GE, Bauer EP, Rodrigues SM, LeDoux JE (2001) Synaptic plasticity in the lateral amygdala: a cellular hypothesis of fear conditioning. Learn Mem 8:229-242.

Brazer SC, Singh BB, Liu X, Swaim W, Ambudkar IS (2003) Caveolin-1 contributes to assembly of store-operated Ca2+ influx channels by regulating plasma membrane localization of TRPC1. J Biol Chem 278:27208-27215.

Chen WR, Xiong W, Shepherd GM (2000) Analysis of relations between NMDA receptors and GABA release at olfactory bulb reciprocal synapses. Neuron 25:625-633.

Clapham DE (2007) SnapShot: mammalian TRP channels. Cell 129:220.

Codazzi F, Di Cesare A, Chiulli N, Albanese A, Meyer T, Zacchetti D, Grohovaz F (2006) Synergistic control of protein kinase Cgamma activity by ionotropic and metabotropic glutamate receptor inputs in hippocampal neurons. J Neurosci 26:3404-3411.

Congar P, Leinekugel X, Ben-Ari Y, Crepel V (1997) A long-lasting calcium-activated nonselective cationic current is generated by synaptic stimulation or exogenous activation of group I metabotropic glutamate receptors in CA1 pyramidal neurons. J Neurosci 17:5366-5379.

Cvetkovic-Lopes V, Eggermann E, Uschakov A, Grivel J, Bayer L, Jones BE, Serafin M, Muhlethaler M (2010) Rat hypocretin/orexin neurons are maintained in a depolarized state by TRPC channels. PLoS One 5:e15673.

Dietrich A, Kalwa H, Storch U, Mederos y Schnitzler M, Salanova B, Pinkenburg O, Dubrovska G, Essin K, Gollasch M, Birnbaumer L, Gudermann T (2007) Pressure-induced and store-operated cation influx in vascular smooth muscle cells is independent of TRPC1. Pflugers Arch 455:465-477.

Dong HW, Heinbockel T, Hamilton KA, Hayar A, Ennis M (2009) Metabotropic glutamate receptors and dendrodendritic synapses in the main olfactory bulb. Ann N Y Acad Sci 1170:224-238.

Egger V (2008) Synaptic sodium spikes trigger long-lasting depolarizations and slow calcium entry in rat olfactory bulb granule cells. Eur J Neurosci 27:2066-2075.

Egger V, Stroh O (2009) Calcium buffering in rodent olfactory bulb granule cells and mitral cells. J Physiol 587:4467-4479.

Egger V, Svoboda K, Mainen ZF (2003) Mechanisms of lateral inhibition in the olfactory bulb: Efficiency and modulation of spike-evoked calcium influx into granule cells. J Neurosci 23:7551-7558.

Egger V, Svoboda K, Mainen ZF (2005) Dendrodendritic synaptic signals in olfactory bulb granule cells: Local spine boost and global low-threshold spike. J Neurosci 25:3521-3530.

El-Hassar L, Hagenston AM, D'Angelo LB, Yeckel MF (2011) Metabotropic glutamate receptors regulate hippocampal CA1 pyramidal neuron excitability via Ca(2) wave-dependent activation of SK and TRPC channels. J Physiol 589:3211-3229.

Fowler MA, Sidiropoulou K, Ozkan ED, Phillips CW, Cooper DC (2007) Corticolimbic expression of TRPC4 and TRPC5 channels in the rodent brain. PLoS One 2:e573.

Freichel M, Suh SH, Pfeifer A, Schweig U, Trost C, Weissgerber P, Biel M, Philipp S, Freise D, Droogmans G, Hofmann F, Flockerzi V, Nilius B (2001) Lack of an endothelial store-operated Ca2+ current impairs agonist-dependent vasorelaxation in TRP4-/- mice. Nat Cell Biol 3:121-127.

Fukunaga I, Yeo CH, Batchelor AM (2007) Potent and specific action of the mGlu1 antagonists YM-298198 and JNJ16259685 on synaptic transmission in rat cerebellar slices. Br J Pharmacol 151:870-876.

Gervasio OL, Whitehead NP, Yeung EW, Phillips WD, Allen DG (2008) TRPC1 binds to caveolin-3 and is regulated by Src kinase - role in Duchenne muscular dystrophy. J Cell Sci 121:2246-2255.

Ghatpande AS, Gelperin A (2009) Presynaptic muscarinic receptors enhance glutamate release at the mitral/tufted to granule cell dendrodendritic synapse in the rat main olfactory bulb. J Neurophysiol 101:2052-2061.

Glitsch MD (2010) Activation of native TRPC3 cation channels by phospholipase D. Faseb J 24:318-325.

Goel M, Sinkins WG, Schilling WP (2002) Selective association of TRPC channel subunits in rat brain synaptosomes. J Biol Chem 277:48303-48310.

Halabisky B, Friedman D, Radojicic M, Strowbridge BW (2000) Calcium influx through NMDA receptors directly evokes GABA release in olfactory bulb granule cells. J Neurosci 20:5124-5134.

Hall BJ, Delaney KR (2002) Contribution of a calcium-activated non-specific conductance to NMDA receptor-mediated synaptic potentials in granule cells of the frog olfactory bulb. J Physiol 543:819-834.

Hartmann J, Henning HA, Konnerth A (2011) mGluR1/TRPC3-mediated Synaptic Transmission and Calcium Signaling in Mammalian Central Neurons. Cold Spring Harb Perspect Biol 3.

Hartmann J, Dragicevic E, Adelsberger H, Henning HA, Sumser M, Abramowitz J, Blum R, Dietrich A, Freichel M, Flockerzi V, Birnbaumer L, Konnerth A (2008) TRPC3 channels are required for synaptic transmission and motor coordination. Neuron 59:392-398.

Head BP, Patel HH, Tsutsumi YM, Hu Y, Mejia T, Mora RC, Insel PA, Roth DM, Drummond JC, Patel PM (2008) Caveolin-1 expression is essential for N-methyl-D-aspartate receptor-mediated Src and extracellular signal-regulated kinase 1/2 activation and protection of primary neurons from ischemic cell death. Faseb J 22:828-840.

Heinbockel T, Laaris N, Ennis M (2007) Metabotropic glutamate receptors in the main olfactory bulb drive granule cell-mediated inhibition. J Neurophysiol 97:858-870.

Hofmann T, Schaefer M, Schultz G, Gudermann T (2002) Subunit composition of mammalian transient receptor potential channels in living cells. Proc Natl Acad Sci U S A 99:7461-7466.

Horne EA, Dell'Acqua ML (2007) Phospholipase C is required for changes in postsynaptic structure and function associated with NMDA receptor-dependent long-term depression. J Neurosci 27:3523-3534.

Isaacson JS (1999) Glutamate spillover mediates excitatory transmission in the rat olfactory bulb. Neuron 23:377-384.

Isaacson JS (2001) Mechanisms governing dendritic gamma-aminobutyric acid (GABA) release in the rat olfactory bulb. Proc Natl Acad Sci U S A 98:337-342.

Isaacson JS, Strowbridge BW (1998) Olfactory reciprocal synapses: dendritic signaling in the CNS. Neuron 20:749-761.

Jahr CE, Nicoll RA (1980) Dendrodendritic inhibition: demonstration with intracellular recording. Science 207:1473-1475.

Kapoor V, Urban NN (2006) Glomerulus-specific, long-latency activity in the olfactory bulb granule cell network. J Neurosci 26:11706-11719.

Kim SJ, Kim YS, Yuan JP, Petralia RS, Worley PF, Linden DJ (2003) Activation of the TRPC1 cation channel by metabotropic glutamate receptor mGluR1. Nature 426:285-291.

Laaris N, Puche A, Ennis M (2007) Complementary postsynaptic activity patterns elicited in olfactory bulb by stimulation of mitral/tufted and centrifugal fiber inputs to granule cells. J Neurophysiol 97:296-306.

Lein ES, Hawrylycz MJ, Ao N, Ayres M, Bensinger A, Bernard A, Boe AF, Boguski MS, Brockway KS, Byrnes EJ, Chen L, Chen L, Chen TM, Chin MC, Chong J, Crook BE, Czaplinska A, Dang CN, Datta S, Dee NR, Desaki AL, Desta T, Diep E, Dolbeare TA, Donelan MJ, Dong HW, Dougherty JG, Duncan BJ, Ebbert AJ, Eichele G, Estin LK, Faber C, Facer BA, Fields R, Fischer SR, Fliss TP, Frensley C, Gates SN, Glattfelder KJ, Halverson KR, Hart MR, Hohmann JG, Howell MP, Jeung DP, Johnson RA, Karr PT, Kawal R, Kidney JM, Knapik RH, Kuan CL, Lake JH, Laramee AR, Larsen KD, Lau C, Lemon TA, Liang AJ, Liu Y, Luong LT, Michaels J, Morgan JJ, Morgan RJ, Mortrud MT, Mosqueda NF, Ng LL, Ng R, Orta GJ, Overly CC, Pak TH, Parry SE, Pathak SD, Pearson OC, Puchalski RB, Riley ZL, Rockett HR, Rowland SA, Royall JJ, Ruiz MJ, Sarno NR, Schaffnit K, Shapovalova NV, Sivisay T, Slaughterbeck CR, Smith SC, Smith KA, Smith BI, Sodt AJ, Stewart NN, Stumpf KR, Sunkin SM, Sutram M, Tam A, Teemer CD, Thaller C, Thompson CL, Varnam LR, Visel A, Whitlock RM, Wohnoutka PE, Wolkey CK, Wong VY, et al. (2007) Genome-wide atlas of gene expression in the adult mouse brain. Nature 445:168-176.

Lisman J, Spruston N (2010) Questions about STDP as a General Model of Synaptic Plasticity. Front Synaptic Neurosci 2:140.

Lockwich TP, Liu X, Singh BB, Jadlowiec J, Weiland S, Ambudkar IS (2000) Assembly of Trp1 in a signaling complex associated with caveolin-scaffolding lipid raft domains. J Biol Chem 275:11934-11942.

Lubke J, Egger V, Sakmann B, Feldmeyer D (2000) Columnar organization of dendrites and axons of single and synaptically coupled excitatory spiny neurons in layer 4 of the rat barrel cortex. J Neurosci 20:5300-5311.

Macrides F, Chorover SL (1972) Olfactory bulb units: activity correlated with inhalation cycles and odor quality. . Science 175:84-87.

Moran MM, Xu H, Clapham DE (2004) TRP ion channels in the nervous system. Curr Opin Neurobiol 14:362-369.

Munsch T, Freichel M, Flockerzi V, Pape HC (2003) Contribution of transient receptor potential channels to the control of GABA release from dendrites. Proc Natl Acad Sci U S A 100:16065-16070.

Odell AF, Scott JL, Van Helden DF (2005) Epidermal growth factor induces tyrosine phosphorylation, membrane insertion, and activation of transient receptor potential channel 4. J Biol Chem 280:37974-37987.

Pace RW, Mackay DD, Feldman JL, Del Negro CA (2007) Inspiratory bursts in the preBotzinger complex depend on a calcium-activated non-specific cation current linked to glutamate receptors in neonatal mice. J Physiol 582:113-125.

Pinato G, Midtgaard J (2003) Regulation of granule cell excitability by a low-threshold calcium spike in turtle olfactory bulb. J Neurophysiol 90:3341-3351.

Pressler RT, Inoue T, Strowbridge BW (2007) Muscarinic receptor activation modulates granule cell excitability and potentiates inhibition onto mitral cells in the rat olfactory bulb. J Neurosci 27:10969-10981.

Riccio A, Li Y, Moon J, Kim KS, Smith KS, Rudolph U, Gapon S, Yao GL, Tsvetkov E, Rodig SJ, Van't Veer A, Meloni EG, Carlezon WA, Jr., Bolshakov VY, Clapham DE (2009) Essential role for TRPC5 in amygdala function and fear-related behavior. Cell 137:761-772.

Salin PA, Lledo PM, Vincent JD, Charpak S (2001) Dendritic glutamate autoreceptors modulate signal processing in rat mitral cells. J Neurophysiol 85:1275-1282.

Schoppa NE, Westbrook GL (1999) Regulation of synaptic timing in the olfactory bulb by an A-type potassium current. Nat Neurosci 2:1106-1113.

Schoppa NE, Kinzie JM, Sahara Y, Segerson TP, Westbrook GL (1998) Dendrodendritic inhibition in the olfactory bulb is driven by NMDA receptors. J Neurosci 18:6790-6802.

Shepherd GM, Greer CA (2004) Olfactory bulb. In: The Synaptic Organization of the Brain, 3rd Edition (Shepherd GM, ed), pp 133-169. New York: Oxford University Press.

Soboloff J, Spassova M, Hewavitharana T, He LP, Luncsford P, Xu W, Venkatachalam K, van Rossum D, Patterson RL, Gill DL (2007) TRPC channels: integrators of multiple cellular signals. Handb Exp Pharmacol:575-591.

Strubing C, Krapivinsky G, Krapivinsky L, Clapham DE (2001) TRPC1 and TRPC5 form a novel cation channel in mammalian brain. Neuron 29:645-655.

Topolnik L, Azzi M, Morin F, Kougioumoutzakis A, Lacaille JC (2006) mGluR1/5 subtype-specific calcium signalling and induction of long-term potentiation in rat hippocampal oriens/alveus interneurones. J Physiol 575:115-131.

Wu LJ, Sweet TB, Clapham DE (2010) International Union of Basic and Clinical Pharmacology. LXXVI. Current progress in the mammalian TRP ion channel family. Pharmacol Rev 62:381-404.

Xue T, Do MT, Riccio A, Jiang Z, Hsieh J, Wang HC, Merbs SL, Welsbie DS, Yoshioka T, Weissgerber P, Stolz S, Flockerzi V, Freichel M, Simon MI, Clapham DE, Yau KW (2011) Melanopsin signalling in mammalian iris and retina. Nature 479:67-73.

Zechel S, Werner S, von Bohlen Und Halbach O (2007) Distribution of TRPC4 in developing and adult murine brain. Cell Tissue Res 328:651-656.

Zelles T, Boyd JD, Hardy AB, Delaney KR (2006) Branch-specific Ca2+ influx from Na+-dependent dendritic spikes in olfactory granule cells. J Neurosci 26:30-40.

Zhang Z, Reboreda A, Alonso A, Barker PA, Seguela P (2011) TRPC channels underlie cholinergic plateau potentials and persistent activity in entorhinal cortex. Hippocampus 21:386-397.

Zheng N, Raman IM (2011) Prolonged postinhibitory rebound firing in the cerebellar nuclei mediated by group I metabotropic glutamate receptor potentiation of L-type calcium currents. J Neurosci 31:10283-10292.

Zhu MX (2005) Multiple roles of calmodulin and other Ca(2+)-binding proteins in the functional regulation of TRP channels. Pflugers Arch 451:105-115.

Zufall F, Ukhanov K, Lucas P, Liman ER, Leinders-Zufall T (2005) Neurobiology of TRPC2: from gene to behavior. Pflugers Arch 451:61-71.

Figure captions Stroh et al.

Figure 1   Synaptically evoked action potentials cause a plateau current in mouse granule cells.

A Scheme of recording configuration (Egger, 2008). Somatically evoked APs (sAP) are generated by current injection, synaptic APs by glomerular stimulation (glAP).

B Two-photon scan of a wild type mouse granule cell filled with 100 μM OGB-1.

C Data recorded from the cell in B. Top trace: Somatic voltage recording of an sAP and a glAP. Note the time course of the afterdepolarization (ADP) for the current-evoked signal vs the long-lasting depolarization (LLD) for the synaptic signal. Bottom traces: Averaged fluorescence transients in response to the above APs recorded in a GC spine and its parent dendrite.

D Scatterplots of LLD vs ADP half duration $t_{1/2}$ and amplitude (top; n = 49 cells) and of the respective fluorescence signals $(\Delta F/F)_{glAP}$ vs $(\Delta F/F)_{sAP}$ (bottom; n = 43 dendrites and spines).

Figure 2   The synaptic plateau current is NMDAR-dependent, but does not require activation of group I mGluRs.

A Individual experiment showing sAP, glAP recorded at the soma and the respective $\Delta F/F$ at a dendritic location under control conditions (black traces) and in 25 μM D-APV (gray traces).

B All APV experiments: Effect of APV on LLD $\tau_{1/2}$ and amplitude (n = 15 cells) and ratios of $(\Delta F/F)_{glAP}$ to $(\Delta F/F)_{sAP}$ for $\tau_{1/2}$ and amplitude (n = 6 locations).

C Top: Individual recording from a granule cell deficient for NR1 (Abraham et al., 2010) showing sAP and glAP. The glAP trace (black) is shown in overlay of the sAP (gray). Bottom: Histogram plot of average ratios of sAP/glAP ADP $\tau_{1/2}$ and amplitude of NR1-deficient GCs (n=5) and WT GCs (n = 49). Error bars represent S.D.

D Top: Individual experiment showing sAP, glAP recorded at the soma under control conditions (black traces) and in the presence of 10 μM YM289189 and 40 μM MPEP (gray traces). Scales as in panel A. Bottom: All experiments with blockade of mGluR1/5: Effect of blockers on LLD $\tau_{1/2}$ and amplitude (n = 5 cells).

Figure 3   **Presence of TRPC4 and TRPC1 in GCs; *TRPC4* deletion reduces the plateau, *TRPC1/4* deletion blocks it.**

A TRPC4 immunoreactivity is detectable in the olfactory GCL in WT mice (a; red) but not in *TRPC1/4/5* triple KO (TKO) mice (b). TRPC1 immunoreactivity is strongly visible in the olfactory GCL in WT mice (c) but not in *TRPC1/4/5* TKO mice (d). DAPI-counterstain in blue. Scale in (d) applies to all.

B Examples for weaker or missing LLDs in *TRPC4-/-, TRPC1/4* DKO and *TRPC1-/-* animals. Averaged traces.

C Distributions of the ratios of sAP/glAP ADP $\tau_{1/2}$ and amplitude for WT and the three different deletions. WT: black columns; *TRPC1-/-*: red line; *TRPC4-/-*: blue line, *TRPC1/4* DKO: purple columns. Indication of overlap regions of WT and DKO distributions via cityscape.

D Summary of the average ratios for all four conditions. For the *TRPC1/4* DKO, the ratio of the sAP-ADP vs the EPSP $\tau_{1/2}$ just below threshold is also shown. The total significance level for the difference between the most unequal values is P < 0.0001 for both ratios (Kruskal-Wallis test). Significance levels of individual results in KO animals versus WT indicated on the respective bars with asterisks and of single KO animals versus DKO with plus signs; +: P < 0.05; ++/** : P < 0.02, *** : P < 0.001, no symbol: not significant (pairwise Mann-Whitney-Tests with Bonferroni-Holm correction).

Figure 4   **TRPC4 and TRPC1 are present in granule cell somata and synapses in the external plexiform layer at the ultrastructural level.**
Ultrastructural analysis using preembedding diaminobenzidine labelling for TRPC4 revealed a strong labelling of the granule cell somata (arrows) in WT mice (**A**) but not

in controls lacking primary antibody incubation (**B**). In higher magnifications of the external plexiform layer (EPL) many immunopositive pre- (arrowheads) and postsynaptic (arrows) profiles are detectable in WT (**C**) but not in controls (**D**).

A similar analysis for TRPC1 revealed a strong labelling of the granule cell somata (arrows) in WT mice (**E**) but not in controls lacking primary antibody incubation (**F**). In higher magnifications of the EPL many immunopositive dendrites are detectable in WT (**G**) but not in controls (**H**).

Figure 5   **The extra Ca^{2+} signal is absent from *TRPC1/4* DKO GCs.**

A Two-photon scan of a representative *TRPC1/4* DKO granule cell.
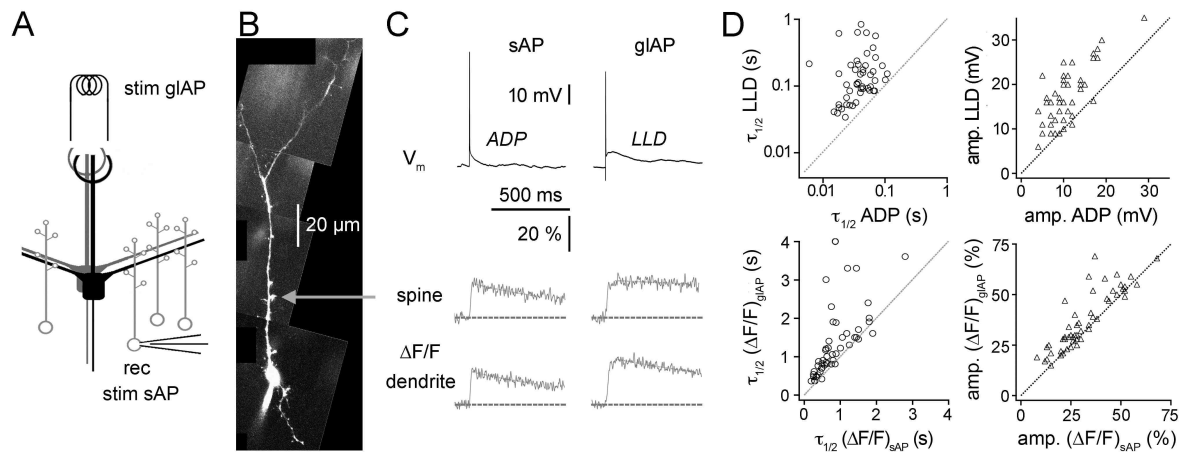
B Analogous to 1C, but data from *TRPC1/4* DKO granule cell. Note the similarity of the responses in comparison to Fig. 1C.

C Scatterplots of glAP-ADP vs sAP-ADP $\tau_{1/2}$ and amplitudes and $(\Delta F/F)_{glAP}$ vs $(\Delta F/F)_{sAP}$ $\tau_{1/2}$ and amplitudes, respectively. The plots show both *TRPC1/4* DKO data (black inverted triangles) and WT data (open symbols, as in Fig. 1) to facilitate comparison (WT n = 43 dendrites and spines, *TRPC1/4* DKO n = 28 dendrites and spines).
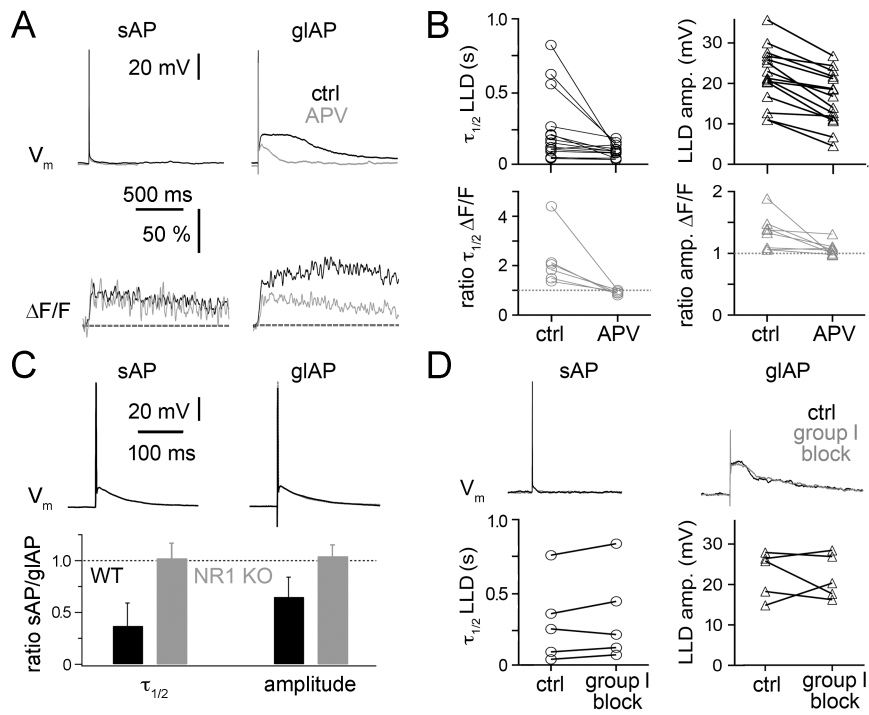
Figure 6   **TRPC channels promote recurrent dendrodendritic inhibition of mitral cells.**

A Scheme of experiment and recordings of reciprocal dendrodendritic inhibition (DDI) in a WT mouse (black) and a *TRPC1/4* DKO mouse (gray) mitral cell.
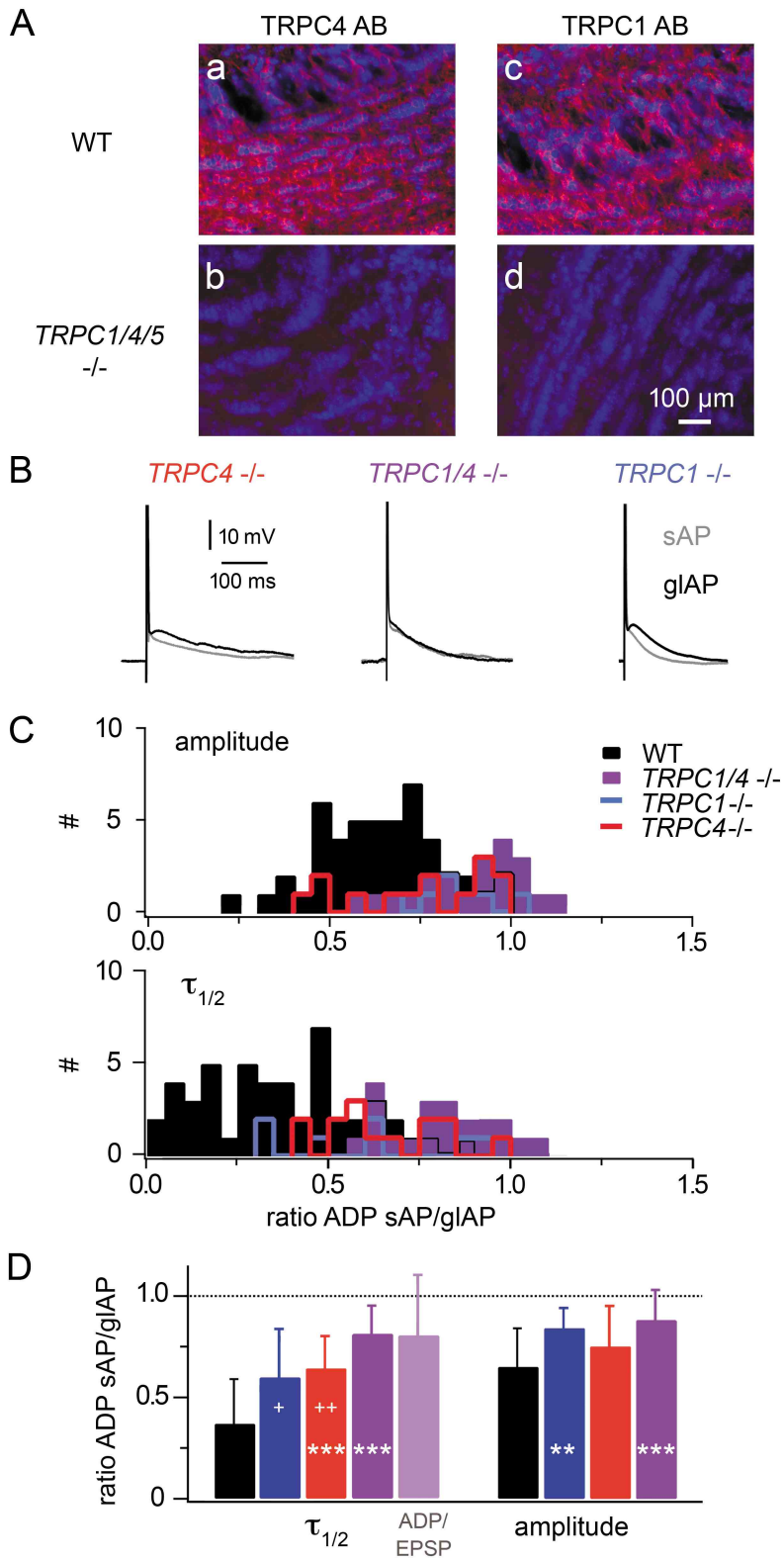
B Averaged DDI recordings for all experiments (n = 7 WT and n = 8 DKO cells). Both the averaged $\tau_{1/2}$ and integral show a significant decrease for the *TRPC1/4* DKO vs WT (P < 0.005 and P < 0.025).
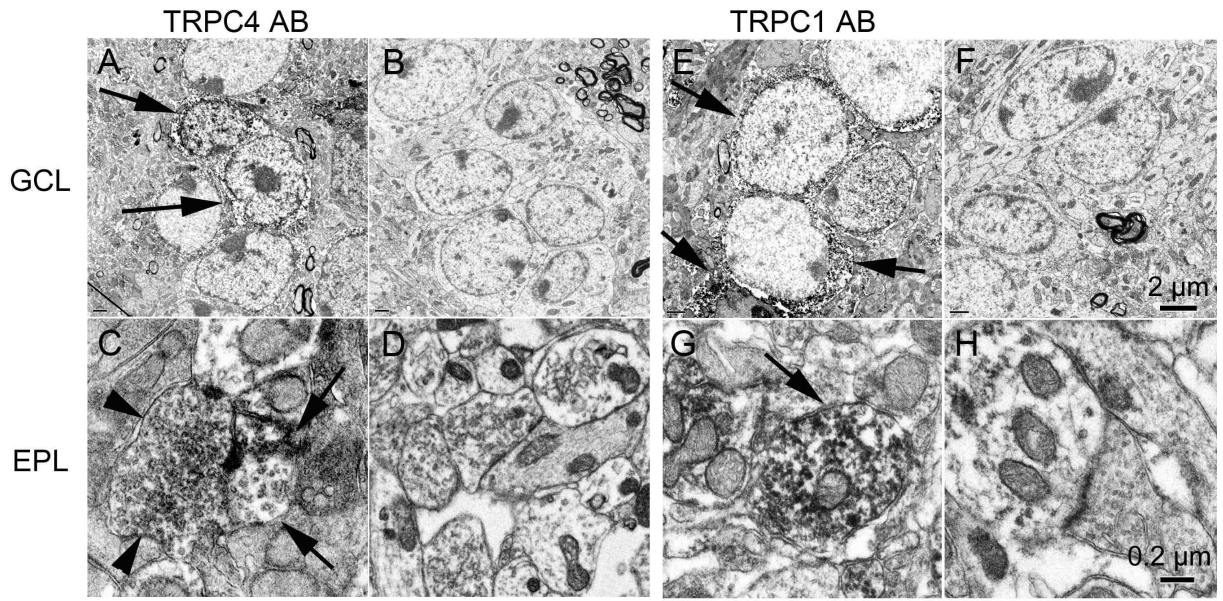
Stroh et al. Fig.1

A

TRPC4 AB   TRPC1 AB

WT

a   c

TRPC1/4/5 -/-

b   d

100 µm

B

TRPC4 -/-   *TRPC1/4 -/-*   *TRPC1 -/-*

10 mV
100 ms

sAP
glAP

C

amplitude

#

WT
TRPC1/4 -/-
TRPC1-/-
TRPC4-/-

$\tau_{1/2}$

#

ratio ADP sAP/glAP

D

ratio ADP sAP/glAP

$\tau_{1/2}$ ADP/
EPSP   amplitude

Stroh et al. Fig. 3

51

TRPC4 AB TRPC1 AB

Stroh et al. Fig. 4

52

Stroh et al. Fig.5

A

0 mV

Vm

20 ms

-70 mV

QX-314

Im

TRPC1/4 -/-
WT

100 pA

200 ms

B
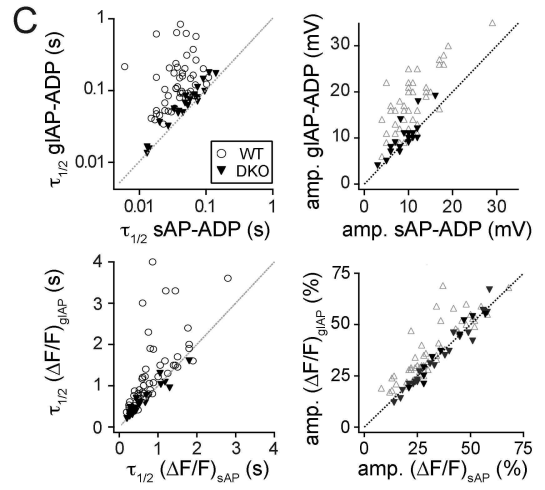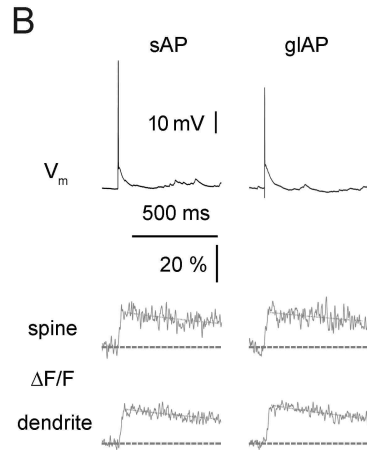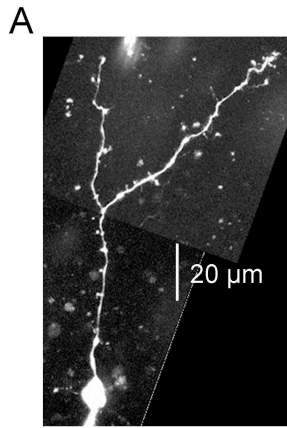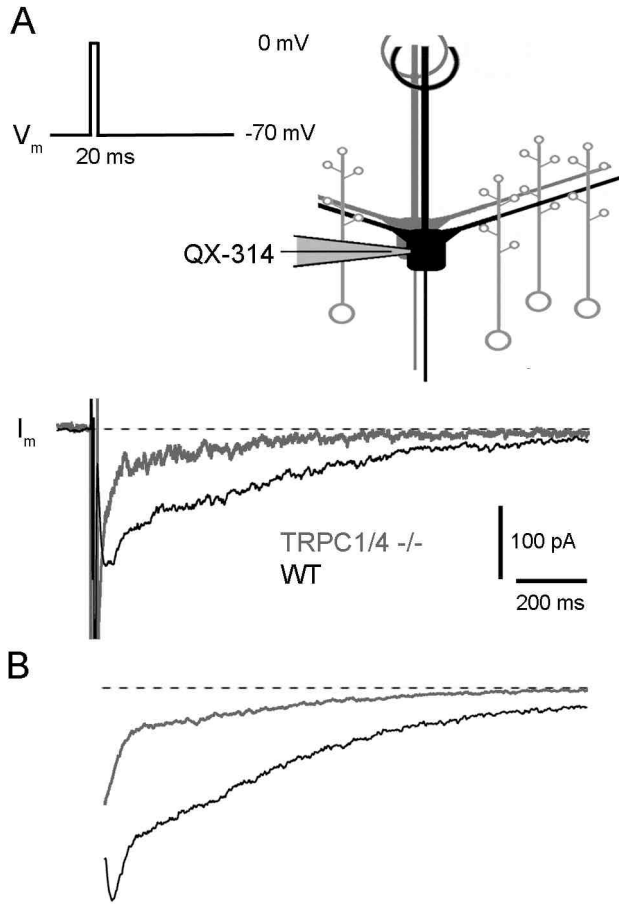
Stroh et al. Fig. 6

Table 1:

Excitability and morphology of *TRPC1/4* DKO granule cells vs WT granule cells

Parameter	WT		*TRPC1/4* DKO		P (Mann-Whitney-Test)
	Mean value ± SD	n	Mean value ± SD	n	
Input resistance	1.07 ± 0.39 GΩ	20	0.89 ± 0.44 GΩ	19	0.14
sAP					
Na$^+$ spike Amplitude	105 ± 10 mV	35	111 ± 16 mV	20	0.08
Na$^+$ spike half width	1.9 ± 0.4 ms	18	2.1 ± 0.4 ms	19	0.11
Number of APs at 50 pA, 800 ms	8.8 ± 3.7	30	7.7 ± 3.8	14	0.24
Synaptic input					
Extracellular stimulation threshold	620 ± 420 μA	35	620 ± 380 μA	23	0.33
Just subthreshold EPSP ▲$_{1/2}$	88 ± 58 ms	39	71 ± 54 ms	21	0.40
Morphology of apical dendrite		25		9	
Length	240 ± 150 μm		215 ± 110 μm		0.67
Number of branchpoints	2.6 ± 1.1		2.0 ± 1.7		0.24

2.2 Calcium buffering in rodent olfactory bulb granule cells and mitral cells

Running title: Ca^{2+} buffering in olfactory bulb granule and mitral cells

Veronica Egger, Olga Stroh

Corresponding author:

Veronica Egger

Institut für Physiologie der LMU, Pettenkoferstr. 12,

80336 München, Germany

Email: V.Egger@lmu.de

Phone: + 49 89 2180 75572

Fax: + 49 89 2180 75512

Abstract

In the mammalian olfactory bulb, axonless granule cells (GCs) mediate self- and lateral inhibitory interactions between mitral cells (MCs) via reciprocal dendrodendritic synapses. Calcium signals in the GC dendrites and reciprocal spines appear to decay unusually slowly, hence GC calcium handling might contribute to the known asynchronous release at this synapse.

By recording fluorescence transients of different Ca^{2+}-sensitive dyes at variable concentrations evoked by backpropagating action potentials (APs) and saturating AP trains we extrapolated Ca^{2+} dynamics to conditions of zero added buffer for juvenile rat GC apical dendrites and spines and MC lateral dendrites.

Resting $[Ca^{2+}]$ was at ~ 50 nM in both GC dendrites and spines. The average endogenous GC buffer capacities κ_e were within a range of 80-90 in the dendrites and 110-140 in the spines. The extrusion rate γ was estimated as 570 s^{-1} for dendrites and 870 s^{-1} for spines and the decay time constant as ~ 200 ms for both. Single current-evoked APs resulted in a $[Ca^{2+}]$ elevation by ~ 250 nM. Calcium handling in juvenile and adult mouse GCs appeared mostly similar.

In MC lateral dendrites, we found AP-mediated $[Ca^{2+}]$ elevations by ~ 130 nM with a similar decay as in GC dendrites, while κ_e and γ were roughly fourfold higher.

In conclusion, the slow GC Ca^{2+} dynamics are due mostly to sluggish Ca^{2+} extrusion. Under physiological conditions this slow removal may well contribute to delayed release and also feed into other Ca^{2+}-dependent mechanisms that foster asynchronous output from the reciprocal spine.

Abbreviations

AP, action potential; CG, Calcium Green; GC, granule cell; κ_E, endogenous buffering capacity; MC, mitral cell; OGB, Oregon Green BAPTA;

Introduction

Olfactory perception appears to be governed by both fast and slow types of temporal coding as investigated in various species and under various conditions of sensory input (review e.g. Wilson & Mainen, 2006). At the level of the olfactory bulb, a special dendrodendritic microcircuit interconnects olfactory bulb granule cells (GCs) and the lateral dendrites of principal mitral cells (MC) and tufted cells via reciprocal GC spines. MC input causes both immediate and asynchronous GC responses, the latter occurring on a 500 ms timescale (Jahr & Nicoll, 1982; Isaacson & Strowbridge, 1998; Schoppa *et al.* 1998). The delayed responses are attributed to mechanisms intrinsic to GCs, such as a transient A-type potassium current I_A (Schoppa & Westbrook, 1999; Kapoor & Urban, 2006) or a non-selective cation current I_{CAN} that requires synaptic activation (Hall & Delaney, 2003; Egger, 2008).

However, there are additional possible sources of delay: Similar to Purkinje neurons (Fierro & Llano 1996), GCs might feature an unusually high buffer capacity since their dendritic calcium signals appear rather sluggish when monitored with calcium-sensitive fluorescent dyes (Egger *et al.* 2003, 2005; Pinato and Midtgaard, 2005; Zelles *et al.* 2006). At physiological temperatures and otherwise similar conditions, GC Ca^{2+} signals decay with a time constant of ~ 400 ms versus ~ 100 ms in neocortical layer 5 and ~ 200 ms in hippocampal CA1 pyramidal cells (Egger *et al.* 2003, 100 µM OGB-1; Markram *et al.* 1995, 100 µM CG-1; Sabatini *et al.* 2002, 100 µM OGB-1). Ca^{2+} clearance is governed mainly by the endogenous buffer capacity κ_E, i.e. the ratio of bound Ca^{2+} to free Ca^{2+} at equilibrium, and the Ca^{2+} extrusion rate γ (Neher and Augustine, 1992; Helmchen *et al.* 1996). Strong intrinsic buffering will reduce the peak local concentration of free Ca^{2+} but prolong the time over which the free Ca^{2+} concentration will remain elevated over baseline. Now if transmitter release was very sensitive to small elevations in free Ca^{2+} concentration, a high κ_E could promote late, asynchronous output. The attenuation of the peak Ca^{2+} concentration may also make release more asynchronous by leaving vesicles available for delayed release. For example there is a long-lasting, low-level component in presynaptic Ca^{2+} signals at the cerebellar granule cell to purkinje cell synapse that is correlated to delayed release (Atluri & Regehr, 1998). Long-lasting presynaptic Ca^{2+} signals were also proposed to

58

underlie asynchronous release from hippocampal cholecystokinin-expressing interneurons (Hefft & Jonas, 2005).

Thus here we investigate a possible contribution of intracellular Ca^{2+} handling to the slow response dynamics of rat granule cells by measuring their endogenous calcium buffer capacity and estimating the time course of their calcium transients under physiological conditions. We also studied Ca^{2+} dynamics at the reciprocal synaptic counterpart of GCs, the MC lateral dendrites. These data both will allow for future modeling studies of Ca^{2+} dynamics and release at the reciprocal synapse and serve as a control for the GC results.

While no gross differences between the mouse and rat olfactory system have been revealed so far, with even a high similarity in the respective odor maps (Soucy *et al.* 2009), calcium handling in mouse GCs might be different, e.g. due to a different distribution of calcium binding proteins similar to what has been shown for the periglomerular neurons in rat and mouse (Kosaka & Kosaka, 2007). Also, there is a large variability emerging across GCs with respect to the expression of calcium binding proteins (see Discussion), and the relative composition of these subtypes might be species-specific. Mouse data play an increasingly important role in olfactory research, and thus we investigated also mouse GC Ca^{2+} dynamics.

Since regular sodium APs elicited by somatic current injection propagate throughout the entire GC dendrite where they cause robust global calcium entry (Egger *et al.* 2003), we used these as a fairly well-defined brief signal to elicit calcium signals in dendrites and spines ("delta function", Helmchen *et al.* 1996), that were monitored with two-photon laser scanning microscopy. Saturating AP trains at two frequencies were used to establish maximal levels of fluorescence and to estimate the resting calcium level and the peak calcium amplitude associated with single current-evoked APs (Maravall *et al.* 2000).

Materials and Methods

All experiments were carried out according to national and institutional guidelines. Animals were briefly anaesthetized with carbon dioxide and decapitated. Sagittal olfactory bulb brain slices were prepared of juvenile Sprague-Dawley rats (thickness 350 μm; postnatal day (PND) 11-16; 60 animals) and B6 mice (thickness 250 μm; PND 16-43; 20 animals).

Neurons were visualized using infrared gradient-contrast illumination via an IR filter (Hoya, Tokyo, Japan) and patched with pipettes 4-8 MΩ in size. Somatic whole cell patch-clamp recordings were performed with an EPC-9 (HEKA, Lambrecht, Germany). Series resistances measured 10-40 MΩ.

The intracellular solution contained [mM]: 130 K-methylsulfate, 10 HEPES, 4 $MgCl_2$, 4 Na_2ATP, 0.4 NaGTP, 10 NaPhosphocreatine, 2 ascorbate, at pH 7.2. The added calcium-sensitive dye was either OGB-1 (20, 50 or 100 μM), OGB-6F (100 μM) or Fluo-5F (100 μM, combined with 25 μM Alexa 594 to visualize the neuronal morphology; all dyes from Invitrogen, Carlsbad, USA). The extracellular artificial cerebrospinal fluid was bubbled with carbogen and contained [mM]: 125 NaCl, 26 $NaHCO_3$, 1.25 NaH_2PO_4, 20 Glucose, 2.5 KCl, 1 $MgCl_2$ and 2 $CaCl_2$. Most experiments were performed at room temperature ($\sim$ 21° C). To check for the effect of physiological temperatures on calcium handling we conducted a subset of experiments where the temperature was raised from 21° C to near-physiological temperatures (32-36° C; temperature control via TC-324B, Warner Instruments, Hamden, USA).

GCs and MCs were identified by their morphological appearance and the shape of their current evoked APs and firing patterns, as evoked via long depolarizing current steps (500 ms) with amplitudes increasing in steps of 10 pA and 50 pA, respectively (Egger *et al.*, 2003; Fig. 1A, Fig. 4A). The average input resistance of the investigated GCs was on the order of 1 GΩ and their resting potential was ranging from -80 to -70 mV, similar to our previous data (Egger *et al.* 2003, Egger 2008). MCs had an input resistance of $\sim$ 200 MΩ and a resting potential range of -60 to -53 mV. Because of the strong expression of LVA calcium channels in GCs (Egger *et al.* 2003; Pinato & Midtgaard, 2003), GCs were generally held within the range given above, whereas MCs were held at -55 to -60 mV. Leaky GCs/MCs that required more than $\sim$ -30 pA/-100 pA

of holding current (i.e. were above spiking threshold) were rejected. Action potentials (APs) were evoked by brief depolarizing somatic current injections (1 ms, 1 nA); saturating trains of APs at 50 and 80 Hz were evoked with 15 successive current injections.

Imaging was performed on an Olympus Fluoview system (Olympus Europe, Hamburg, Germany), with two-photon excitation at 800 nm provided by a Ti:Sapphire solid-state laser system (Mai Tai, Spectraphysics, Mountain View, CA, USA). The microscope was equipped with a 60x Nikon fluor water immersion objective (NA 1.0; Nikon Instruments, Amstelveen, The Netherlands). Fluorescence transients in response to somatically evoked APs were imaged in line-scan mode (temporal resolution 2 ms) at different locations along the apical dendrite of GCs, usually within the external plexiform layer, and within its spines or along a lateral dendrite of a MC. Mostly we used rather proximal dendritic locations (10-100 μm from the soma) to make sure that the calcium dye concentration had equilibrated at the imaged location (see also Fig. 1 C). For MCs we waited at least 30 – 40 min before imaging. Fluorescence transients in response to single APs were recorded at a stimulus repetition rate of 0.1 Hz. Saturating fluorescence signals in response to AP trains were imaged at yet lower rates below 0.03 Hz; otherwise, the fluorescence signals in response to the following trains would often decrease in amplitude.

Changes in calcium were measured in absolute terms f_0, f_i and for comparison between experiments in terms of $\Delta F/F = \delta f = (f_i - f_o) / f_0$. The average background fluorescence was calculated from an adjacent region of the same width as the imaged structure and subtracted from f_0. Since erroneous background correction can result in considerable distortions (Sabatini *et al.* 2002), the possibility of such influences was analysed carefully (Fig. 5).

Measurement of absolute Ca^{2+} according to Maravall et al. (2000)
Absolute Ca^{2+} levels were measured according to the method by Maravall *et al.* (2000). We used trains of 15 APs at 80 Hz and 50 Hz, respectively, to establish the saturation correction factor x (eq. 2; Fig. 1B). The K_d of OGB-1 at room temperature was assumed

to be ~ 200 nM, in accordance with literature values (e.g. Maravall *et al.* 2000; Wilms *et al.* 2006; Stocca *et al.* 2008; Hendel *et al.* 2008; see results section for effects of a possible intracellular reduction in dye K_d). The intracellular dynamic range R_f of OGB-1 was assumed to be on the order of 6 (Maravall *et al.* 2000).

For Fluo-5F, K_d was assumed as 1300 nM (at room temperature, 1 mM Mg^{2+}: Woodruff *et al.* 2002).

Absolute $[Ca^{2+}]_i$ was determined from the fluorescence level f_i via

$$[Ca^{2+}]_i = K_d \cdot (f_i/f_{max} - 1/R_f)/(1 - f_i/f_{max}) \qquad \text{(eq. 1; *Maravall et al. 2000*)}$$

with the maximal fluorescence f_{max} estimated via the saturating fluorescence measured at two frequencies ($\nu_1 < \nu_2$; here $\nu_1 = 50$ Hz and $\nu_2 = 80$ Hz), using the saturation factor x:

$$f_{max} = f_{max}\_\nu_2 \cdot 100/x$$
$$x = 100 \cdot (1 - (\delta f_{max}\_\nu_2/ \delta f_{max}\_\nu_1) \cdot (\nu_1/\nu_2))/(1 - (\nu_1/\nu_2)) \quad \text{(eq. 2, *Maravall et al. 2000*)}$$

The contribution to the total buffer capacity from the dye κ_B was estimated as:

$$\kappa_B = (K_d \cdot [c_{dye}])/((K_d + [Ca^{2+}]_o) \cdot (K_d + [Ca^{2+}]_{AP})) \quad \text{(eq. 3; *Augustine & Neher, 1992*)}$$

The extrapolation of the measured decay time constants τ and peak amplitude changes in absolute calcium $\Delta[Ca^{2+}]_{AP}$ to conditions of zero added buffer in a single compartment allows to get two independent estimates of the endogenous buffer capacity κ_B, with :

$$\tau = (1 + \kappa_E + \kappa_B)/\gamma$$

$$\text{(eq. 4; *Helmchen et al. 1996*)}$$
$$\Delta[Ca^{2+}]_{AP} = \Delta[Ca^{2+}]_{TOTAL}/(1 + \kappa_E + \kappa_B)$$

The extrusion rate γ reflects the removal of Ca^{2+} from the cytosol via ionic pumps and exchangers.

While 50 Hz trains in mitral cells would always contain only full-blown APs, some mitral cells were not quite able to respond with full APs to current injections at 80 Hz even at the maximally available current, resulting in a decrease in AP amplitude within the train and thus also a reduced Ca^{2+} entry that would not surpass the plateau level at 50 Hz stimulation. In these cases, we calculated the maximal fluorescence based on the maximal fluorescence measured at 50 Hz and the saturation factor as determined from other mitral cells. Similarly, if in GCs we encountered a decrease in δf_{max_v} in the course of recording several trains and/or could not obtain good measurements at both 50 Hz and 80 Hz, we would use only the first measurement and then estimate f_{max} based on x measured in other GCs.

Data analysis and selection

Data were analyzed with custom software based on Igor (Wavemetrics, Lake Oswego, OR, USA). For kinetic analysis, we used only averaged transients with small noise levels after slight smoothing (3-5 point wide sliding window). The decay of all $\Delta F/F$ signals was determined in terms of their half duration time $\tau_{1/2}$ rather than in terms of the exponential decay time constant τ to keep them comparable to the dynamics of other GC Ca^{2+} signals that decay in a non-exponential fashion (Egger *et al.* 2005; Zelles *et al.* 2006; Egger 2008). For the final estimate of calcium dynamics under physiological conditions (physiological temperature, no added dye), the decay time constant was calculated via $\tau = \ln(2) \bullet \tau_{1/2}$.

After analysis of the absolute $[Ca^{2+}]_i$ levels in all experiments the OGB-1 data were selected for the final extrapolation according to the following criteria:
(1) $\delta f_{max} > 150$ %. Low values of δf_{max} might indicate bleaching or other photodamage (Maravall *et al.* 2000). In our measurements from rat GCs, OGB-1 showed an average $\delta f_{max} = 205 \pm 27$ % (range 160 – 256; n = 85 dendrites and spines).

63

(2) resting calcium $[Ca^{2+}]_o < 100$ nM. This criterion was meant to ensure cellular health, since we found an average $[Ca^{2+}]_o \approx 50$ nM (see Results).

(3) κ_B no less than 20 % below the average κ_B at the given indicator concentration. While incomplete equilibration was not a problem in the majority of experiments due to rapid filling of the small granule cells (see also Results, Fig. 1), sometimes the recording pipette might have become clogged, resulting in a block of further exchange of pipette solution and cytosol. Data were subjected to particular scrutiny if both κ_B and $\tau_{1/2}$ were low, a hallmark of insufficient equilibration (see eq. 4).

(4) a regular firing pattern as described in Egger *et al.* (2003). We also encountered cells that had the morphological appearance of GCs but bursting or fast-spiking firing patterns (n = 4 for each type). Most of these cells showed Ca^{2+} dynamics that were obviously different from those in GCs with regular firing, with much larger $\Delta[Ca^{2+}]_{AP}$; thus we excluded all of them from the sample ($\Delta[Ca^{2+}]_{AP}$ on average 177 ± 117 % larger than in the regularly spiking GCs, n = 20 dendrites and spines).

Estimates of the ratio of spine and parent dendritic radius

To estimate the relative diameter of spines and their parent dendrites, we used the full width at half maximum (FWHM) of the structures in the averaged projection of the line scans onto their spatial dimension after background subtraction. Although most imaged structures are on a size scale comparable to the resolution level of our two-photon microscope (lateral resolution $\delta r = 0.4 \cdot \lambda_{exc} / NA = 0.3$ µm) and therefore cannot be resolved faithfully, this procedure yielded a mean radius for GC spines that is very close to the published electronmicroscopic data (0.46 ± 0.08 µm (n=26) *vs.* 0.51 ± 0.07 µm from Woolf *et al.* 1991). The mean ratio of spine and dendritic radius was then used to estimate their relative surface-to-volume ratios. We also estimated the radius of the MC lateral dendrites (0.86 ± 0.26 µm, n = 23).

Statistics

To assess statistical significance levels, the nonparametric Wilcoxon matched-pairs signed-ranks test was applied for comparing paired data sets. Unpaired data were compared via the Mann-Whitney test. The significance of correlations was tested using

the Spearman correlation coefficient. All averages are given ± S.D. unless indicated otherwise.

Results

Calcium signals in rat granule cell dendrites and spines

As noted previously (Egger *et al.* 2003), the small size of GCs promoted rapid filling with the dye via the patch pipette. Single action potentials evoked by somatic current injection resulted in detectable fluorescence increases for all dyes and dye concentrations used in this study. Usually, the fluorescence signals at locations close to the cell soma would equilibrate within less than 10 minutes, showing no more decrease in amplitude and simultaneous increase in decay time constants (Fig. 1C). Therefore we were not able to observe regular loading curves and extrapolate the endogenous buffer capacity for individual cell locations (as e.g. in Maravall *et al.* 2000); rather, we would wait for 10-15 min and then collect data for different dye concentrations, extrapolating endogenous buffer capacities and unperturbed transients for an ensemble of cells. If these data showed any indication of incomplete loading (see Methods), they were excluded from the final analysis.

The resting Ca^{2+} concentration as calculated via eq. 1 is independent of the concentration of added dye due to homeostatic mechanisms and therefore can be averaged over all data sets. GC $[Ca^{2+}]_0$ thus was estimated to be 51 ± 11 nM in dendrites (n = 53) and 49 ± 12 nM in spines (n = 39).

To estimate the maximal possible fluorescence level f_{max} in a given compartment, we applied saturating trains of APs at frequencies of 50 and 80 Hz (Fig. 1B). A larger plateau fluorescence was obtained for the latter frequency, allowing us to calculate the degree of saturation x and obtain the maximal fluorescence by applying the correction $f_{max} = f_{max}\_80Hz/x$ according to Maravall *et al.* (2000). We found a saturation factor of 85 ± 7 % S.D. (n = 40 dendritic locations) for plateau levels δf_{max}_80Hz, in close agreement with the saturation factor determined by Maravall *et al.* at 83 Hz ($85 \pm 4\%$ S.E.M.).

A decrease in δf_{max} in the course of a measurement was also taken as a warning that the location might have become photodamaged, since such decreases occurred in particular upon repetitive recording and imaging of trains at short intervals. These observations lead us to use an interval of > 30 s between the recordings of AP trains and rather low illumination levels for the final measurements presented here.

Extrapolation of GC data to conditions of zero added buffer

We measured Ca^{2+} dynamics in response to single APs and AP trains in GC spines and dendrites loaded with different indicators at varying concentrations (OGB-1 at 20 µM, 11

spines and 20 dendrites in 9 cells; OGB-1 at 50 μM, 14 spines and 18 dendrites in 9 cells; OGB-1 at 100 μM, 15 spines and 15 dendrites in 11 cells; Fluo-5F at 100 μM in 15 spines and 10 dendrites in 11 cells). Representative data for each of the OGB-1 concentrations are shown in Fig. 1. The decay time constants for $(\Delta F/F)_{AP}$ were averaged over data from these and additional cells to reduce the inherently large standard deviation. For the OGB-1 data we also determined absolute Ca^{2+} levels at rest and at the AP peak, yielding $\Delta[Ca^{2+}]_{AP}$.

The Fluo-5F data did not allow for a proper measurement of absolute Ca^{2+} levels because the resting Ca^{2+} could not be determined with this medium-affinity dye. Thus we used only the measured decay half durations, estimating $\kappa_{B\_Fluo} \approx 66$. Exclusion of the Fluo-5F data from the extrapolation did not significantly change the result.

Fig. 2 shows the extrapolation for both dendrites and spines, for the inverse $\Delta[Ca^{2+}]_{AP}$ and τ respectively plotted versus the added buffer capacity κ_B. Both x-axis intercepts yield the endogenous buffer capacity κ_B while the y-axis intercepts yield the values of $\Delta[Ca^{2+}]_{AP}$ and τ at 0 added buffer, and the extrusion rate γ is the inverse of the slope of the fit. The results are given in Table 1.

TABLE 1: Extrapolation results and estimate of extrusion rate in juvenile rat granule cell apical dendrites and spines

Parameter	Spine (total n = 55)		Dendrite (total n = 63)	
	Mean	SDdatafit	Mean	SDdatafit
21° C				
κ_E via τ	138	100	87	55
κ_E via $\Delta[Ca^{2+}]_{AP}$	107	75	85	13
$\tau_{1/2}$_RT (ms)	250	90	250	120
$\Delta[Ca^{2+}]_{AP}$ (nM)	250	120	230	33
γ_RT (s^{-1})	550	340	360	150
37° C				
τ_0_PT (ms)	175	60	175	80
γ_PT (s^{-1})	870	540	570	240
γ_0_PT (μm/s)	150	90	170	70

TABLE legend: Total numbers are given including the Fluo-5F data. The standard deviations were calculated via propagation of the SDs of the fit parameters. The extrusion rate γ was estimated via $\gamma = (1 + \kappa_E)/\tau$.

The estimate of τ at physiological temperatures (τ_PT) is based on the previously measured $Q_{10\_\tau} \approx 0.63$: τ_PT = τ_RT•$(Q_{10\_\tau})^{\Delta T/10}$ (Egger *et al.* 2003; see also Lee *et al.* 2004). If we assume that the temperature dependence of κ_E is weak (e.g. Helmchen *et al.* 1997), then γ_PT will increase with $1/Q_{10\_\tau}$ in relation to γ_RT. This relation is also in accordance with the temperature dependence of extrusion mechanisms. For example the Na$^+$Ca^{2+} exchanger has a $Q_{10\_NaCa} \approx 1.57$ (from Shannon *et al.* 2004), so its inverse is $1/Q_{10\_NaCa} \approx 0.64$. The Q_{10} of γ in other preparations was also found within a similar range (e.g. $Q_{10} \approx 2$, Helmchen *et al.* 1997; $Q_{10} \approx 1.7$, Stocca *et al.* 2008). The amplitude of $\Delta[Ca^{2+}]_{AP}$ is likely to be fairly independent of temperature changes, except for a slight decrease in peak $[Ca^{2+}]_{AP}$ due to the shorter duration of the action potential ($Q_{10} \approx 0.9$, Markram *et al.* 1995; Lee *et al.* 2004). We verified these assumptions by measuring $[Ca^{2+}]_0$, $\Delta[Ca^{2+}]_{AP}$ and $\tau_{1/2}$ at the same location at both room temperature and near-physiological temperatures (32-36° C; n = 5 locations in 3 GCs and n =

3 locations in 2 MCs). In both cell types $[Ca^{2+}]_0$ was temperature-independent while $\Delta[Ca^{2+}]_{AP}$ showed a slight decrease to ~ 80% of its value at room temperature and $\tau_{1/2}$ decreased to ~ 50%, yielding a similar $Q_{10}\_\tau_{1/2} \approx 0.6$ as used above. Thus κ_E is weakly temperature-dependent; most of the dependence is carried by extrusion. For the estimate of the intrinsic extrusion rate γ_0 see next section.

We also performed measurements in 9 GCs using 100 µM of the low-affinity dye OGB-6F ($K_d \approx 2.2 – 3$ µM, Holthoff *et al.* 2004; Invitrogen Handbook). Cells were bright enough at the resting potential to visualize dendrites and individual spines. While low-affinity dyes cannot detect $[Ca^{2+}]_0$ and require substantial averaging for the measurement of small signals such as $(\Delta F/F)_{AP}$, the decay time course of $\Delta F/F$ will resemble unperturbed Ca^{2+} dynamics. The averaged $(\Delta F/F)_{AP}$ signals yielded average decay half durations very similar to the extrapolated time course at zero added buffer, namely $\tau_{1/2} = 270 \pm 80$ ms at 13 dendritic locations, and $\tau_{1/2} = 250 \pm 70$ ms in 9 spines. An example is shown in Fig. 2C.

Granule cell spines versus dendrites

While the extrapolated $\Delta[Ca^{2+}]_{AP}$ and $\tau_{1/2}$ as shown in Table 1 are very similar in spines and dendrites, the large standard deviation might obscure a systematic difference in individual pairs of spines and their parent dendrites. The ratio of the respective values in spines *vs.* parent dendrites are shown in Fig. 2B. The extrapolation of the mean ratios to zero added buffer yields a ratio of 0.94 ± 0.38 for $\Delta[Ca^{2+}]_{AP}$ and a ratio of 0.79 ± 0.19 for τ_0, indicating a similar amplitude of $\Delta[Ca^{2+}]_{AP}$ and a slightly faster decay of the signal in GC spines versus their parent dendrites, as would be expected due to their larger surface-to-volume ratio (SVR).

The SVR is required to estimate the intrinsic extrusion rate $\gamma_0 = \gamma/SVR$. The SVR is 3/r for a spherical spine and 2/r for a cylindrical dendrite. While GC spines are often ellipsoidal rather than spherical and highly variable in their shape, their average surfaces can be described fairly well by a sphere with an effective radius of 0.51 ± 0.07 µm based on electron-microscopic data from mouse GCs (at PND 30,35; Woolf *et al.* 1991a). Since there is little quantitative anatomical data on the radius of GC apical dendrites ($1.0 – 1.2$ µm proximal to $0.4 – 0.6$ µm distal, Woolf *et al.* 1991b), we estimated the ratio of spinous to dendritic surfaces in the spines of our data set by measuring the ratio of the apparent width of spines and their parent dendrites in the line scans, 0.85 ± 0.23 in rat (n = 26 pairs; see Methods) and 0.80 ± 0.22 in

mouse (n = 13). Together with the electronmicroscopic data cited above, these data led us to assume a mean effective spine radius of 0.5 μm and a mean effective dendritic radius of 0.6 μm for both species. These assumptions yielded intrinsic extrusion rates that are roughly equal for GC dendrites and spines (see Table 1).

Juvenile and adult Mouse GCs

Absolute Ca^{2+} concentrations in mouse GCs (Fig. 3) were measured as described before in two sets of cells filled with 100 μM OGB-1, the first from mice aged PND16-23 and the second from mice aged PND 36-43 (10 *vs.* 14 cells). The two age groups were not significantly different from each other with regard to $[Ca^{2+}]_0$, κ_B and $\tau_{1/2}$, while there was a slight decrease in $\Delta[Ca^{2+}]_{AP}$ with age in the dendrites (P < 0.05, Mann-Whitney test, 10 *vs.* 9 locations). A similar but not quite significant decrease was also seen in the spines (P = 0.09). Therefore, the data from both age groups were pooled together, resulting in an average dendritic $[Ca^{2+}]_0 = 51 \pm 11$ nM (n = 18) and spine $[Ca^{2+}]_0 = 50 \pm 11$ nM (n = 31). For all buffer-dependent parameters, i.e. $\Delta[Ca^{2+}]_{AP}$, κ_B and $\tau_{1/2}$, Fig. 3C shows the comparison of the respective rat data relative to the mouse data. There were no significant differences except for $\Delta[Ca^{2+}]_{AP}$ in the mouse spines, which was on average 40% smaller than in rat at the same indicator concentration (Mann-Whitney test, P < 0.025; see also Fig. 2B). Due to this overall similarity between rat and mouse data for 100 μM OGB-1, we did not perform additional experiments in mouse GCs at other dye concentrations.

Rat mitral cells

To characterize Ca^{2+} handling at the opposite side of the dendrodendritic synapse, we also investigated mitral cell Ca^{2+} buffering. In addition, these data serve as a control for our results in granule cells.

For MCs we used similar concentrations of the indicator OGB-1 as for GCs (at 20 μM, 16 dendritic locations in 5 cells; at 50 μM, 15 locations in 4 cells; at 100 μM, 16 locations in 4 cells). The large MCs required longer filling for equilibration; measurements even next to the MC soma were made at least 30 min after break in. Again, if MC data showed any indication of incomplete loading (see also methods), they were not used for the final analysis. The resting Ca^{2+} concentration as calculated via eq. (1) was averaged over all data sets. $[Ca^{2+}]_0$ thus was estimated to be 55 ± 11 nM in lateral MC dendrites (n = 44 locations). The saturation factor was x = 84 ± 7 % SD (n = 21 dendritic locations) for plateau levels measured at 80 Hz.

Fig. 4 shows a representative experiment and the extrapolation. Its results are given in Table 2. While both the MC buffer capacity and extrusion rate are considerably higher than in GCs, these changes cancel out when it comes to the extrapolated decay half duration. Therefore, the decay of Ca^{2+} signals in GCs and MCs is likely to be similar also under physiological conditions. The mitral cell lateral dendrites in our data set had an estimated radius of 0.86 ± 0.26 µm, yielding a SVR = 2.3 µm^{-1}.

TABLE 2 Extrapolation results and estimate of extrusion rate in juvenile rat mitral cell lateral dendrites

Parameter	Mean	SD
21° C		
κ_E via τ	400	390
κ_E via $\Delta[Ca^{2+}]_{AP}$	360	340
$\tau_{1/2}\_RT$ (ms)	270	90
$\Delta[Ca^{2+}]_{AP}$ (nM)	130	40
γ_RT (s^{-1})	1470	1360
37° C		
τ_0_PT (ms)	190	60
γ_PT (s^{-1})	3060	2830
γ_0 (µm/s)	1320	1220

Analysis of background influence and other sources of error and variability

The dark noise level of our detection system at the used photomultiplier tube voltage and gain was on the order of 30 arbitrary units (total dynamic range 4096). The majority of our data sets had a background no more than two times above the dark noise level (including the dark noise; background/dark noise = 2.2 ± 1.1, n = 51) and was also small in relation to the basal fluorescence level of the imaged structures (f_0/background = 6.5 ± 3.9). To control for an erroneous manipulation of the raw data by background subtraction (Sabatini *et al.* 2002) we tested whether there was a systematic relationship between the background level and the measured parameters $[Ca^{2+}]_0$, κ_B and peak $[Ca^{2+}]_{AP}$. To obtain a data set large enough to reveal possible correlations, the individual data for κ_B and peak $[Ca^{2+}]_{AP}$ for the different

concentrations of OGB-1 were normalized to their mean values, yielding a total of 48 dendritic and 36 spine data points. Fig. 5 shows that no significant correlations were found.

The intracellular environment is likely to lower the affinities K_d of the dyes, resulting in higher actual $[Ca^{2+}]$ levels that scale directly with K_d (eq. 1). κ_B will scale inversely with K_d (eq. 3) and thus for a given increase in K_d we obtain similar decreases in κ_E. Therefore our results for the endogenous buffering capacity κ_E represent an upper limit, while the absolute $[Ca^{2+}]$ concentrations represent a lower limit. Variations in R_f affect the results more weakly: an increase in R_f by 25% will cause a 7% reduction in buffering capacity and a 16% increase in absolute Ca^{2+} concentrations. If we used $R_f = 8.5$ as an upper limit (Maravall *et al.* 2000), κ_E would decrease by 10%.

Another potential source of variability is the existence of various subtypes of GCs (see Discussion); the observed GCs with irregular firing patterns that were excluded from the sample (see Methods) may represent correlates of such subtypes.

Discussion

Granule cell and mitral cell Ca²⁺ handling and dendritic release

The present extrapolation of GC Ca^{2+} dynamics to conditions of zero added buffer allows for two main conclusions. First, there is little difference in Ca^{2+} handling between the GC spine and the dendrite with respect to all extrapolated parameters (see below). Second, the apparently slow dynamics observed in previous measurements are not due to a particularly high GC endogenous buffer capacity. GC κ_E is within a medium range (~100), not as low as in hippocampal or cortical pyramidal cell fine dendrites and spines (range 20 – 60, Maravall *et al.* 2000; Sabatini *et al.* 2002; Cornelisse *et al.* 2007), and not as high as in Purkinje cells (~ 2000, Fierro and Llano, 1996) or cortical layer 2/3 inhibitory interneurons (~ 300, Kaiser *et al.* 2001) and hippocampal basket cells (~ 200, Aponte *et al.* 2008). The apparently slow decay of GC calcium signals is rather caused by a comparably low extrusion rate γ (600 - 900 s^{-1}) at physiological temperatures, whereas extrusion in most of the other mentioned neuronal types was found to be at least two times faster.

Thus GC Ca^{2+} signalling under physiological conditions is likely to occur on an intermediate timescale ($\tau \approx 175$ ms; see Fig. 6). Isaacson and Strowbridge (1998) and Schoppa *et al.* (1998) measured a time constant of asynchronous release from GCs of $\tau_{as} \approx 500$ ms at room temperature; its Q_{10} was sampled in a small set of experiments as 2.3 $\pm$ 0.7 (n = 3; Isaacson & Strowbridge, 1998), yielding a physiological time scale of $\tau_{as}\_PT \approx 150$ ms. Thus a main conclusion from our data is that asynchronous release from the GC spine is likely to be fostered by the slow removal of Ca^{2+} from the cytosol. Delayed release may be also triggered in conjunction with mechanisms of slow Ca^{2+} entry into the GC spine, e.g. due to activation of I_{CAN} (Hall & Delaney, 2003; Egger, 2008).

Is there a general correlation between κ_E and asynchrounous release, in the sense that medium to higher buffering capacities may favor delayed release? This hypothesis is difficult to test for two reasons: there is scant data available regarding κ_E at synapses with delayed release, and there are also other tightly intertwined parameters that factor into the relation between Ca^{2+} influx and release, such as the speed of

buffering, the size of the relevant domain, the affinity of the calcium sensor and the degree of coupling between Ca^{2+} entry and Ca^{2+} sensor. For example, asynchronous release might be favored by high buffering capacities (Atluri & Regehr, 1998) and/or parvalbumin expression (Collin *et al.* 2005); however, reduced Ca^{2+} buffering increased asynchronous release in rod bipolar cells (Singer & Diamond 2003), and parvalbumin-expressing hippocampal interneurons are less prone to asynchronous release than cholecystokinin-expressing interneurons (Hefft and Jonas, 2005). Our own data also do not support such a relation, since MC lateral dendrites show a considerably higher κ_E than GC spines while there are no reports of asynchronous release at the dendrodendritic MC to GC synapse. Nevertheless a κ_E in the medium to high range may be necessary - but not sufficient - to sustain asynchronous release.

While we found Ca^{2+} dynamics in mitral cell dendrites to occur on a similar timescale as in GC dendrites and spines, the underlying mechanisms operate in a quite different manner, with a rather high κ_E (~ 400) and an accordingly high extrusion rate (~ 3000; see Fig. 6B). Perhaps these differences contribute to the contrasting forms of short-term plasticity that were observed at the MC-GC synapse and the GC-MC synapse (Diez & Murthy, 1995). Previous Ca^{2+} imaging data in mitral cell in the main and accessory olfactory bulb showed also fairly slow AP-mediated transients within the lateral and apical dendrites including the tuft (Xiong & Chen, 2002; Ma & Lowe, 2004; Urban & Castro, 2004; note the apparently biphasic tuft signals in Yuan & Knöpfel, 2006).

The considerable variability in the MC data is most likely due to the tapering of the MC lateral dendrites in our data set, reflected in the large standard deviation in their dendritic diameter.

GC spines and dendrites

We find that granule cell spines and dendrites have rather similar Ca^{2+} handling properties. There is no apparent specialization of the reciprocal GC spine that may be related to its input/output function as compared to the dendrite. Interestingly, the electronmicroscopic data indicate that there are varicosities on GC dendritic shafts that also bear reciprocal synapses (Woolf *et al.* 1991a); the density of these shaft synapses is

74

not known. Morphologically, the dimensions of a GC spine are comparable to a 1 µm-section of parent dendrite and thus GC spines and dendrites also resemble each other in this respect. However, there could be a differential distribution of mobile buffers that becomes washed out in the whole-cell configuration used here.

In hippocampal CA1 neurons, Ca^{2+} handling in spines and small, distal dendrites was also found to be fairly similar to each other (Fig. 6; Table 1 in Sabatini *et al.* 2002), whereas spine Ca^{2+} kinetics were faster and κ_E lower by a factor of 2 in cortical pyramidal cells (Cornelisse *et al.* 2007). Compared to GC spines, both hippocampal and cortical spines show a considerably higher Ca^{2+} influx. This is likely to be due to their smaller size (see e.g. Cornelisse *et al.* 2007): GC spines have a 6fold larger surface and a 10fold larger volume than hippocampal spines (Woolf *et al.* 1991a). Fig. 6A illustrates this point by showing the relative anatomical sizes of an "average" GC spine and dendrite, a mitral cell lateral dendrite and a CA1 cell spine and dendrite (Harris & Stevens, 1989) and the sizes of their average Ca^{2+} signals due to backpropagating APs.

Sources of variability

While our two data sets on τ and $\Delta[Ca^{2+}]_{AP}$ converge quite well onto similar values of κ_E for both GC dendrites and spines and MC dendrites, there is a considerable variability of the data across cells. Some may be due to errors in the measurement process such as insufficient dye equilibration. Another possible source of variability is the existence of various GC subtypes, both with respect to the expression of Ca^{2+} binding proteins (CaBPs) and their maturational state, since GCs are subject to constant turnover (Bayer 1985).

First, the expression of CaBPs in olfactory bulb GCs is variable and also species-specific. In rodents, some GCs express calretinin, and a non-overlapping subset expresses neurocalcin. αCaMKII is heavily expressed and NCS-1 is also widespread among GCs, whereas calbindin is at best weakly expressed and parvalbumin was not found (e.g. Brinon *et al.* 1999; Toida *et al.* 1996; Zou *et al.* 2002; Treloar *et al.* 2005).

Second, maturation might well include changes in Ca^{2+} buffering as shown e.g. for hippocampal and cerebellar interneurons or retinal ganglion cells (Stocca *et al.* 2008; Collin *et al.* 2005; Mann *et al.* 2005). While the GCs in our sample appeared

mature with respect to their anatomy and AP firing (Carleton *et al.* 2002), there might be more subtle gradations of maturation that affect Ca^{2+} handling.

Another consequence of GC turnover is the coexistence of early born and adult born cells. These two populations have been found to differ with respect to certain physiological properties (Lledo *et al.* 2008) and thus may also differ in Ca^{2+} handling. While our juvenile rat data are restricted to early-born GCs simply because of the young age of the animals, the mouse data may encompass both early-born and adult-born neurons.

Outlook and conclusion

The parameters we have measured will help to interpret measurements of population activity from olfactory bulb neurons that have been either bulk-loaded with indicator or express genetically encoded indicators (e.g. Stosiek *et al.* 2003; Hendel *et al.* 2008) and thus contribute to the analysis of *in vivo* observations of olfactory processing. Mathematical approaches (e.g. Borst & Abarbanel, 2007) may allow to extrapolate unperturbed GC Ca^{2+} signals where Ca^{2+} entry - unlike in the case of backpropagating, current-evoked APs – does not resemble a δ-function, such as during low-threshold spikes or synaptic calcium entry within a spine (Egger *et al.* 2005; Egger, 2008).

In conclusion, GC Ca^{2+} dynamics are slow under physiological conditions, owing mostly to sluggish Ca^{2+} extrusion. This slow clearance of Ca^{2+} from the cytoplasm may contribute to delayed release and also feed into other Ca^{2+}-dependent mechanisms that foster asynchronous output from the reciprocal spine. Conversely, extrusion from mitral cell lateral dendrites is relatively fast while their buffer capacity is high.

References

Aponte Y, Bischofberger J & Jonas P (2008). Efficient Ca2+ buffering in fast-spiking basket cells of rat hippocampus. *J Physiol* **586**, 2061-2075.

Atluri PP & Regehr WG (1998). Delayed release of neurotransmitter from cerebellar granule cells. *J Neurosci* **18**, 8214-8227.

Bayer SY (1985). Neuron production in the hippocampus and olfactory bulb of the adult rat brain: addition or replacement? *Ann N Y Acad Sci* **457**, 163-172.

Brinon JG, Martinez-Guijarro FJ, Bravo IG, Arevalo R, Crespo C, Okazaki K, Hidaka H, Aijon J & Alonso JR (1999). Coexpression of neurocalcin with other calcium-binding proteins in the rat main olfactory bulb. *J Comp Neurol* **407**, 404-414.

Borst A, Abarbanel HD (2007). Relating a calcium indicator signal to the unperturbed calcium concentration time-course. *Theor Biol Med Model* **4**, 7.

Carleton A, Petreanu LT, Lansford R, Alvarez-Buylla A & Lledo PM (2003). Becoming a new neuron in the adult olfactory bulb. *Nat Neurosci* **6**, 507-518.

Collin T, Chat M, Lucas MG, Moreno H, Racay P, Schwaller B, Marty A & Llano I (2005). Developmental changes in parvalbumin regulate presynaptic Ca2+ signaling. *J Neurosci* **25**, 96-107.

Cornelisse LN, van Elburg RA, Meredith RM, Yuste R & Mansvelder HD (2007). High speed two-photon imaging of calcium dynamics in dendritic spines: consequences for spine calcium kinetics and buffer capacity. *PLoS ONE* **2**, 1073.

Dietz SB & Murthy VN (2005). Contrasting short-term plasticity at two sides of the mitral-granule reciprocal synapse in the mammalian olfactory bulb. *J Physiol* **569**, 475-488.

Egger V, Svoboda K & Mainen ZF (2003). Mechanisms of lateral inhibition in the olfactory bulb: efficiency and modulation of spike-evoked calcium influx into granule cells. *J Neurosci* **23**, 7551-7558.

Egger V, Svoboda K & Mainen ZF (2005). Dendrodendritic synaptic signals in olfactory bulb granule cells: local spine boost and global low-threshold spike. *J Neurosci* **25**, 3521-3530.

Egger V (2008). Synaptic sodium spikes trigger long-lasting depolarizations and slow calcium entry in rat olfactory bulb granule cells. *Eur J Neurosci* **27**, 2066-2075.

Fierro L & Llano I (1996). High endogenous calcium buffering in Purkinje cells from rat cerebellar slices. *J Physiol* **496**, 617-625.

Hall BJ & Delaney KR (2002). Contribution of a calcium-activated non-specific conductance to NMDA receptor-mediated synaptic potentials in granule cells of the frog olfactory bulb. *J Physiol* **543,** 819-834.

Harris KM & Stevens JK (1989). Dendritic spines of CA 1 pyramidal cells in the rat hippocampus: serial electron microscopy with reference to their biophysical characteristics. *J Neurosci* **9**, 2982-2997.

Hefft S & Jonas P (2005). Asynchronous GABA release generates long-lasting inhibition at a hippocampal interneuron-principal neuron synapse. *Nat Neurosci* **8**, 1319-1328.

Helmchen F, Imoto K & Sakmann B (1996). Ca^{2+} buffering and action potential-evoked Ca^{2+} signaling in dendrites of pyramidal neurons. *Biophys J* **70**, 1069-1081.

Helmchen F, Borst JG & Sakmann B (1997). Calcium dynamics associated with a single action potential in a CNS presynaptic terminal. *Biophys J* **72**, 1458-1471.

Hendel T, Mank M, Schnell B, Griesbeck O, Borst A & Reiff DF (2008). Fluorescence changes of genetic calcium indicators and OGB-1 correlated with neural activity and calcium in vivo and in vitro. *J Neurosci* **28**, 7399-7411.

Isaacson JS & Strowbridge BW (1998). Olfactory reciprocal synapses: dendritic signaling in the CNS. *Neuron* **20**, 749-761.

Jahr CE & Nicoll RA (1982). Noradrenergic modulation of dendrodendritic inhibition in the olfactory bulb. *Nature* **297**, 227-229.

Kaiser KM, Zilberter Y & Sakmann B (2001). Back-propagating action potentials mediate calcium signalling in dendrites of bitufted interneurons in layer 2/3 of rat somatosensory cortex. *J Physiol* **535**, 17-31.

Koester HJ & Sakmann B (2000). Calcium dynamics associated with action potentials in single nerve terminals of pyramidal cells in layer 2/3 of the young rat neocortex. *J Physiol* **529**, 625-646.

Kosaka K & Kosaka T (2007). Chemical properties of type 1 and type 2 periglomerular cells in the mouse olfactory bulb are different from those in the rat olfactory bulb. *Brain Res* **1167**, 42-55.

Lee JC, Callaway JC & Foehring RC (2005). Effects of temperature on calcium transients and Ca2+-dependent afterhyperpolarizations in neocortical pyramidal neurons. *J Neurophysiol* **93**, 2012-2020.

Lledo PM, Merkle FT & Alvarez-Buylla A (2008). Origin and function of olfactory bulb interneuron diversity. *Trends Neurosci* **31**, 392-400.

Ma J & Lowe G (2004). Action potential backpropagation and multiglomerular signaling in the rat vomeronasal system. *J Neurosci* **24**, 9341-9352.

Mann M, Haq W, Zabel T, Guenther E, Zrenner E & Ladewig T (2005). Age-dependent changes in the regulation mechanisms for intracellular calcium ions in ganglion cells of the mouse retina. *Eur J Neurosci* **22**, 2735-2743.

Maravall M, Mainen ZF, Sabatini BL & Svoboda K (2000). Estimating intracellular calcium concentrations and buffering without wavelength ratioing. *Biophys J* **78**, 2655-2667.

Markram H, Helm PJ & Sakmann B (1995). Dendritic calcium transients evoked by single back-propagating action potentials in rat neocortical pyramidal neurons. *J Physiol* **485**, 1-20.

Neher E & Augustine GJ (1992). Calcium gradients and buffers in bovine chromaffin cells. *J Physiol* **450**, 273-301.

Pinato G & Midtgaard J (2005). Dendritic sodium spikelets and low-threshold calcium spikes in turtle olfactory bulb granule cells. *J Neurophysiol* **93**, 1285-1294.

Sabatini BL, Oertner TG & Svoboda K (2002). The life cycle of Ca^{2+} ions in dendritic spines. *Neuron* **33**, 439-452.

Shannon TR, Wang F, Puglisi J, Weber C & Bers DM (2004). A mathematical treatment of integrated Ca dynamics within the ventricular myocyte. *Biophys J* **87**, 3351-3371.

Singer JH & Diamond JS (2003). Sustained Ca^{2+} entry elicits transient postsynaptic currents at a retinal ribbon synapse. *J Neurosci* **23**, 10923-10933.

Soucy ER, Albeanu DF, Fantana AL, Murthy VN & Meister M (2009). Precision and diversity in an odor map on the olfactory bulb. *Nat Neurosci* **12**, 210-220.

Stocca G, Schmidt-Hieber C & Bischofberger J (2008). Differential dendritic Ca^{2+} signalling in young and mature hippocampal granule cells. *J Physiol* **586**, 3795-3811.

Stosiek C, Garaschuk O, Holthoff K, Konnerth A (2003) In vivo two-photon calcium imaging of neuronal networks. *Proc Natl Acad Sci U S A* **100**, 7319-7324.

Toida K, Kosaka K, Heizmann CW & Kosaka T (1996). Electron microscopic serial-sectioning/reconstruction study of parvalbumin-containing neurons in the external plexiform layer of the rat olfactory bulb. *Neuroscience* **72**, 449-466.

Treloar HB, Uboha U, Jeromin A & Greer CA (2005). Expression of the neuronal calcium sensor protein NCS-1 in the developing mouse olfactory pathway. *J Comp Neurol* **482**, 201-216.

Urban NN & Castro JB (2005). Tuft calcium spikes in accessory olfactory bulb mitral cells. *J Neurosci* **25**, 5024-5028.

Wilms CD, Schmidt H & Eilers J (2006). Quantitative two-photon Ca^{2+} imaging via fluorescence lifetime analysis. *Cell Calcium* **40**, 73-79.

Wilson RI & Mainen ZF (2006). Early events in olfactory processing. *Ann Rev Neurosci* **29**, 163-201.

Woodruff ML, Sampath AP, Matthews HR, Krasnoperova NV, Lem J & Fain GL (2002). Measurement of cytoplasmic calcium concentration in the rods of wild-type and transducin knock-out mice. *J Physiol* **542**, 843–854.

Woolf TB, Shepherd GM & Greer CA (1991a). Serial reconstructions of granule cell spines in the mammalian olfactory bulb. *Synapse* **7**, 181-192.

Woolf TB, Shepherd GM & Greer CA (1991b). Local information processing in dendritic trees: subsets of spines in granule cells of the mammalian olfactory bulb. *J Neurosci* **11**, 1837-1854.

Xiong W & Chen WR (2002). Dynamic gating of spike propagation in the mitral cell lateral dendrites. *Neuron* **34**, 115-126.

Yasuda R, Nimchinsky EA, Scheuss V, Pologruto TA, Oertner TG, Sabatini BL & Svoboda K (2004). Imaging calcium concentration dynamics in small neuronal compartments. *Sci STKE* **03**, 2004(219):pl5.

Yuan Q & Knöpfel T (2006). Olfactory nerve stimulation-induced calcium signaling in the mitral cell distal dendritic tuft. *J Neurophysiol* **95**, 2417-2426.

Zelles T, Boyd JD, Hardy AB & Delaney KR (2006). Branch-specific Ca^{2+} influx from Na+-dependent dendritic spikes in olfactory granule cells. *J Neurosci* **26**, 30-40.

Zou DJ, Greer CA & Firestein S (2002). Expression pattern of alpha CaMKII in the mouse main olfactory bulb. *J Comp Neurol* **443**, 226-236.

Figure Legends

Figure 1: Fluorescence transients ΔF/F in granule cells in response to single current evoked APs and AP trains. Fast equilibration.

A Two-photon scan of a granule cell filled with 100 μM OGB-1 and somatic voltage recordings of this cell's reponse to 500 ms depolarizing pulses (white traces at the bottom). Scaling of the voltage trace similar to traces in B.

B Somatic voltage recordings and corresponding averaged fluorescence transients ΔF/F imaged in line scan mode across the proximal dendrite and a spine of the cell shown in A. The decay half duration $\tau_{1/2}$ was 650 ms in the dendrite and 430 ms in the spine. Left, responses to single APs $(\Delta F/F)_{AP}$; on the right, responses to trains of 15 APs at 50 and 80 Hz, all evoked by somatic current injection. Scaling of all traces as indicated by the bars; note the condensed scaling of the ΔF/F responses to AP trains.

C Examples of averaged $(\Delta F/F)_{AP}$ responses from two other granule cell dendrites, filled with 50 μM and 20 μM OGB-1 respectively, and recorded at the indicated times after break-in. Scaling of the voltage recordings and $(\Delta F/F)_{AP}$ transients similar as above.

Figure 2: Extrapolation to conditions of 0 added buffer for granule cell dendrites and spines; data with low-affinity dye.

A Top graphs: Extrapolation of decay half duration data versus exogenous buffer capacity in dendrites and spines. Bottom: Inverse of absolute change $\Delta[Ca^{2+}]$ per single somatic AP. Straight lines: linear fit, dotted lines: 2σ confidence interval, dashed lines: 1σ confidence interval. These intervals do not account for the uncertainty in the data points themselves. All error bars represent SEMs. The errors in x-direction (SEM of mean κ_B) are very small and thus not visible.

B Relation of spine to dendrite $\Delta[Ca^{2+}]_{AP}$ (◆) and of $\tau_{1/2}$ (▢) of individual pairs of spines and their parent dendrites versus the concentration of OGB-1 (9 pairs for each data point). The open symbols represent data from mouse (16 pairs). The lines represent linear fits of the rat data, the error bars again represent SEMs.

C Representative data for the low-affinity dye OGB-6F. About 20 averaged traces for

ΔF/F. The decay half duration was $\tau_{1/2} \approx 200$ ms for the dendrite and $\tau_{1/2} \approx 240$ ms for the adjacent spine. The inset shows a scan of the respective granule cell with the scale bar corresponding to 10 µm; the data shown were recorded from the upper spine next to the GC soma.

Figure 3: Ca²⁺ handling in mouse granule cells.

A Two-photon scan of a mouse granule cell (PND 36) filled with 100 µM OGB-1 and somatic voltage recordings of this cell's reponse to 500 ms depolarizing pulses (white trace). Scaling of the voltage trace similar to traces in B.

B Somatic voltage recordings and simultaneous fluorescence transients ΔF/F imaged in line scan mode across the proximal dendrite and a spine of the cell shown in A. Depiction as in Fig. 1 B.

C Comparison between mouse and rat data for dendrites (D) and spines (S); all using 100 µM OGB-1. The rat data were normalized to 100%. The mouse data are shown as relative fractions and included 24 GCs of mice aged PND16-43.

Figure 4: Ca²⁺ handling in juvenile rat mitral cells. Extrapolation to conditions of 0 added buffer.

A Two-photon scan of rat mitral cells (PND 14) filled with 100 µM OGB-1 and somatic voltage recordings of the left cell's reponse to 500 ms depolarizing pulses (white trace). Scaling of the voltage trace similar to traces in B.

B Somatic voltage recordings and simultaneous fluorescence transients ΔF/F imaged across the lateral dendrite shown in A, at the positions labeled *1* and *2*. Depiction as in Fig. 1 B.

C Data points from recordings with 20, 50 and 100 µM OGB-1. Top graph: extrapolation of decay half duration data *vs.* total buffer capacity in mitral cell lateral dendrites. Bottom: Inverse of absolute change $\Delta[Ca^{2+}]$ per single somatic AP. Straight lines: linear fit, dotted lines: 2σ confidence interval, dashed lines 1σ confidence interval. These intervals do not account for the uncertainty in the data points themselves. All error bars represent S.E.M.s. The errors in x-direction (S.E.M. of mean kappa) are very small and thus barely visible.

Figure 5: Influence of background levels on $[Ca^{2+}]_0$, peak $[Ca^{2+}]$ and κ_B.

Measurements of $[Ca^{2+}]_0$, peak $[Ca^{2+}]$ and κ_B for OGB-1 in individual locations in GC dendrites (top row) and spines (bottom row) versus the fluorescence background measured next to these locations. The lines indicate the linear fits, r the Spearman correlation coefficient and P the significance of the difference between the determined r and r = 0 (no correlation). The shown data include all GC OGB-1 measurements at 20, 50 and 100 μM; to heighten the sensitivity to possible correlations, peak $[Ca^{2+}]$ and κ_B were normalized to their average value at the concentration at hand and pooled.

Figure 6: Estimated average Ca^{2+} dynamics under physiological conditions in granule cells, mitral cell lateral dendrites and hippocampal CA1 cells.

This figure illustrates the estimated mean dimensions and the extrapolated Ca^{2+} dynamics of the investigated structures (GC spine and dendrite, MC lateral dendrite; Table 1 and Table 2) and a spine on a fine hippocampal pyramidal cell dendrite for comparison. The olfactory bulb anatomical data were in part taken from Woolf *et al.* (1991a; see Methods and Results). The hippocampal data were taken from Harris and Stevens (1989) and Sabatini *et al.* (2002; their Table 1), respectively. The black traces show the mean Ca^{2+} transient, the grey band denotes the SD with respect to $\Delta[Ca^{2+}]_{AP}$ and τ. Panel B shows the extrapolated buffer capacities and extrusion rates for GC spines and dendrites and MC lateral dendrites under physiological conditions.
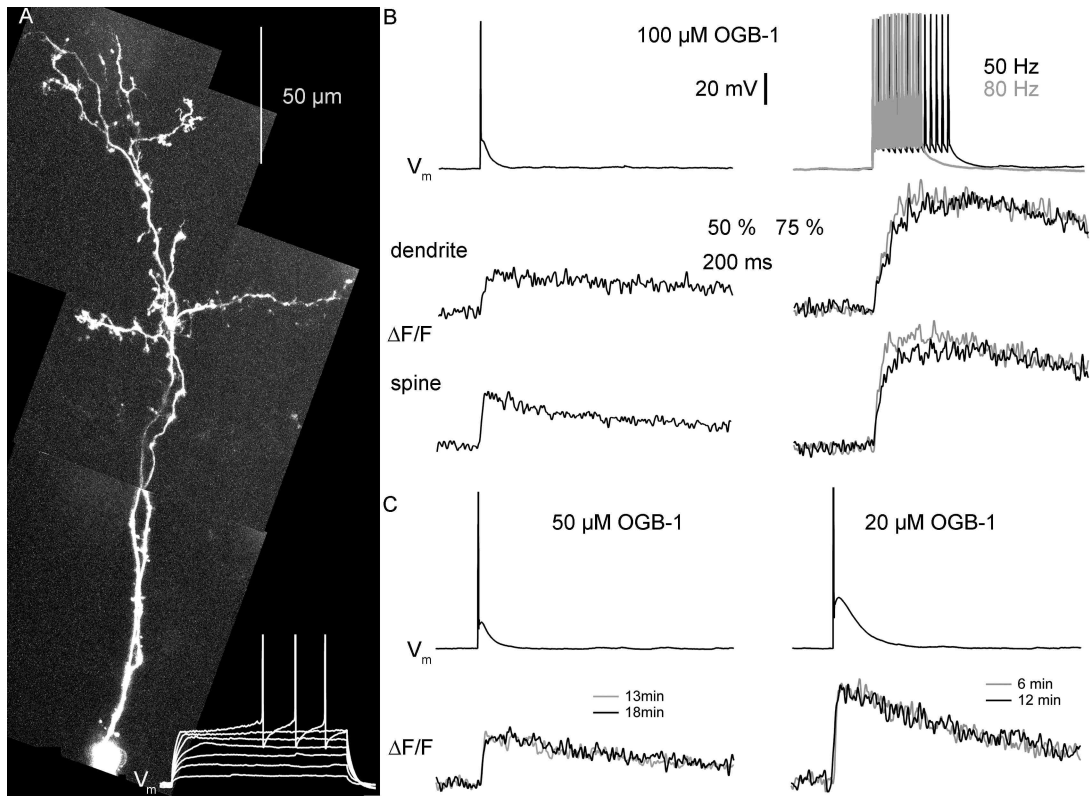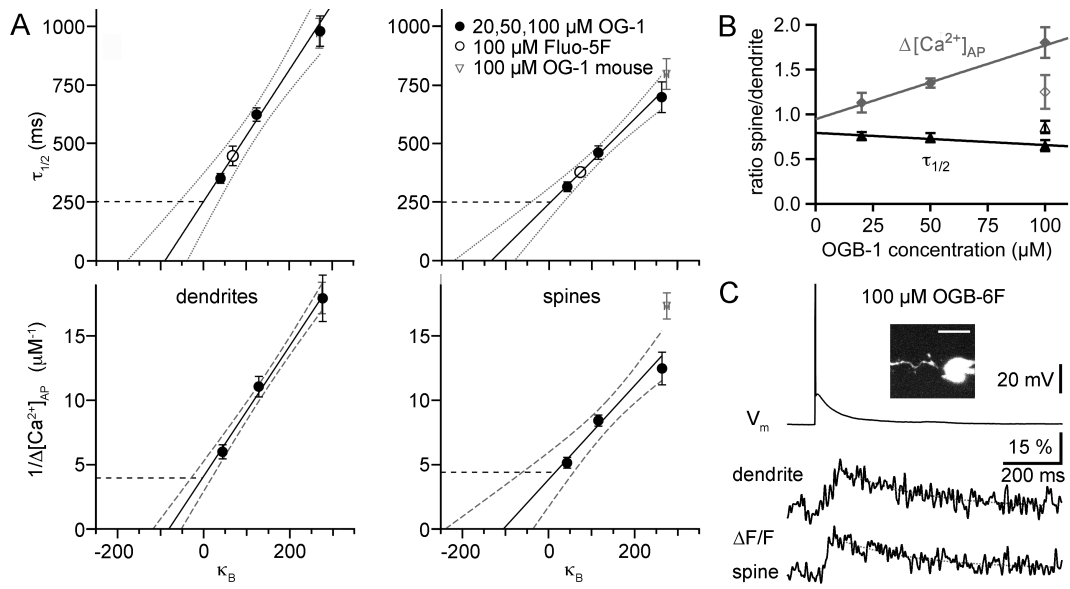
A

B

100 µM OGB-1

20 mV

50 Hz
80 Hz

V_m

dendrite

50 %   75 %
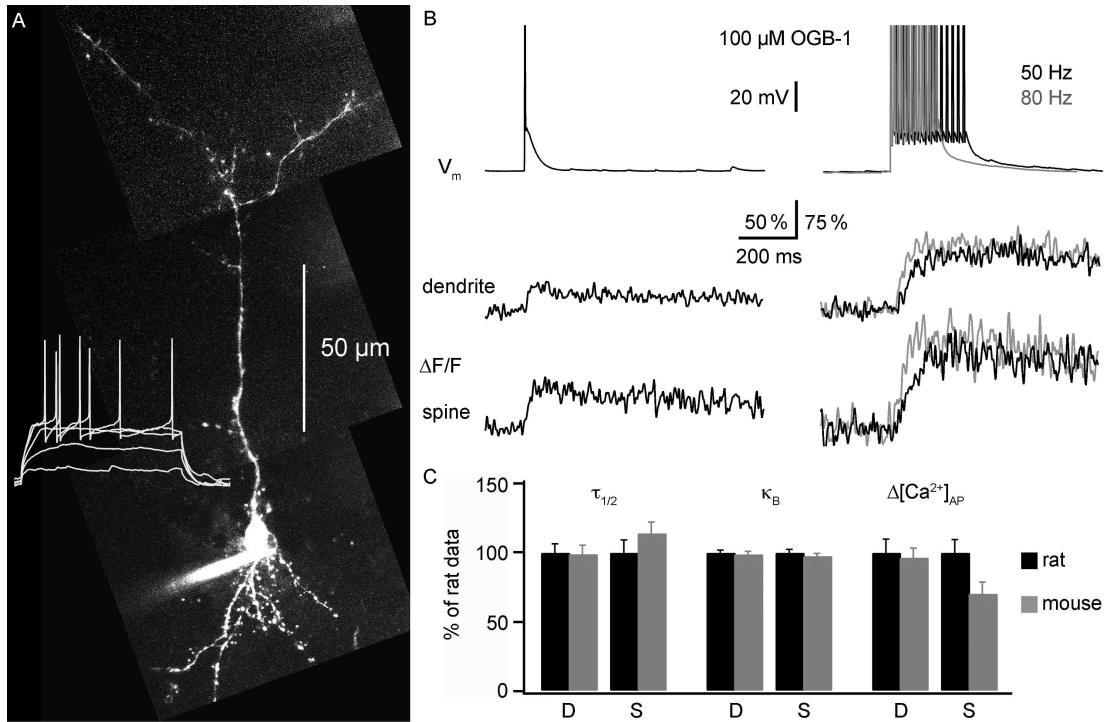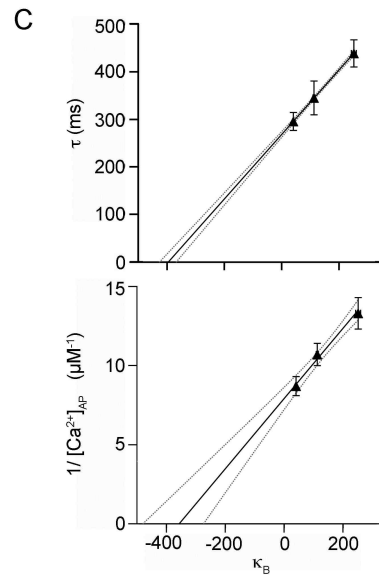200 ms

ΔF/F

spine

C

50 µM OGB-1

20 µM OGB-1

V_m

13min
18min

6 min
12 min

ΔF/F

Figure 1
Egger & Stroh

87

Figure 2
Egger&Stroh

A

B
100 µM OGB-1

20 mV

50 Hz
80 Hz

V_m

50 % 75 %
200 ms

dendrite

$\Delta F/F$

spine

C

$\tau_{1/2}$ κ_B $\Delta[Ca^{2+}]_{AP}$

% of rat data

150

100

50

0

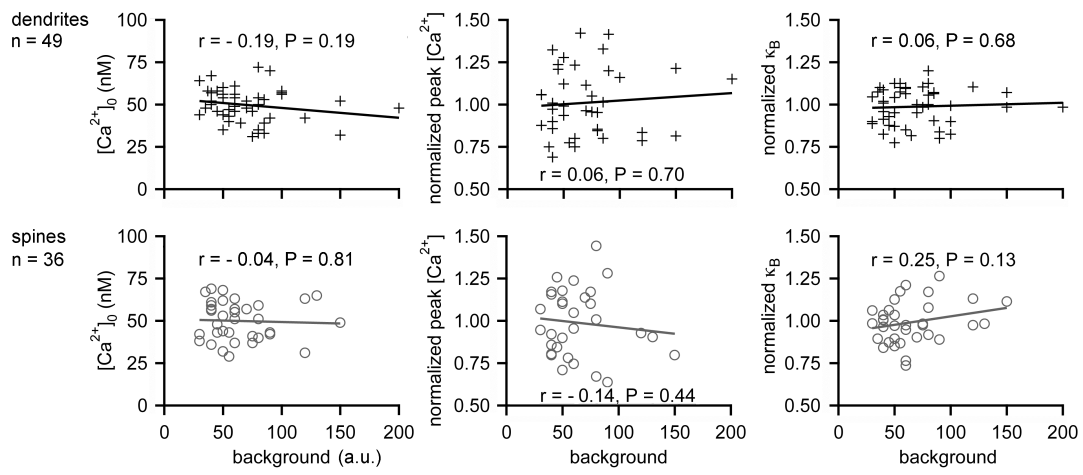D   S   D   S   D   S

rat
mouse

Figure 3
Egger & Stroh

89
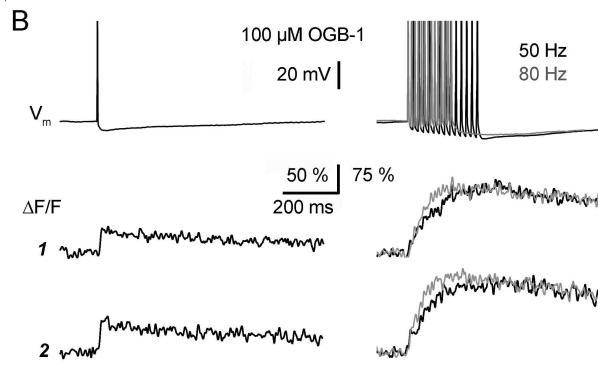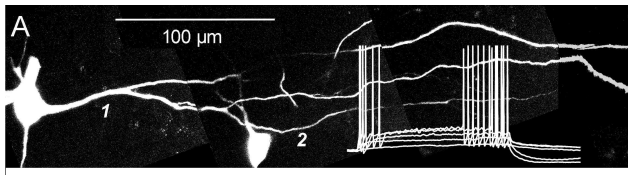
Figure 4
Egger & Stroh

Figure 5
Egger & Stroh

91

A   granule cell

B   mitral cell lateral dendrite

C   hippocampal pyramidal cell
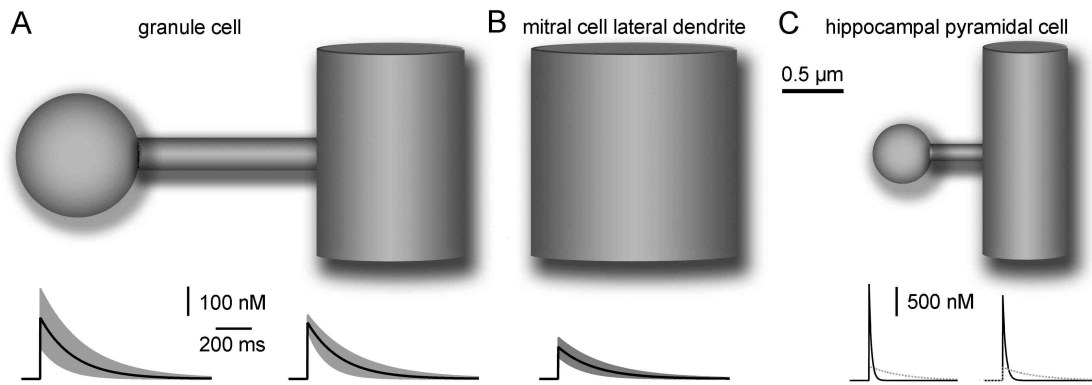
| 100 nM
—
200 ms

0.5 µm

| 500 nM

Figure 6
Egger & Stroh

Veröffentlichungen

Stroh O., Freichel M., Kretz O, Birnbaumer L., Hartmann J. & Egger V. NMDA-receptor dependent synaptic activation of TRPC channels in olfactory bulb granule cells. J Neurosci. (Zum Druck angenommen Januar 2012)

Egger V. & Stroh O. Calcium buffering in rodent olfactory bulb granule cells. *J Physiol* **587**: 4467-4479 (2009)

Konferenzbeiträge

Egger V., Stroh O., Mainen Z.F. & Konnerth A. Synaptic spikes in olfactory bulb granule cells cause long-lasting depolarization and calcium entry. *85. Jahrestagung DPG,* OT3-15 (2006)

Egger V., Stroh O., Mainen Z.F. & Konnerth A. Synaptic spikes in olfactory bulb granule cells cause long-lasting depolarization and calcium entry. *FENS Abstr.* **5**, A074.6 (2006)

Egger V. & Stroh O. Calcium handling in rodent olfactory bulb granule cells. *FENS Abstr.* 6 (2008)

Egger V. & Stroh O. Calcium handling in rodent olfactory bulb granule cells. *ECRO 2008 Abstr. 51* (2008)

Egger V. & Stroh O. A possible role for TRPC channels in olfactory bulb granule cell synaptic signalliing. *Proc. 8th Göttingen Conference Ger. Neurosci.* **5,** T5-4C (2009)

Egger V. & Stroh O. A role for TRPC channels in synaptic dendritic Ca2+ signals of olfactory bulb granule cells. *Gordon Conference on "Dendrites"* (2009)

Stroh O., Freichel M., Hartmann J., Egger V. TRPC channels modulate reciprocal mitral cell-granule cell signaling in the olfactory bulb. . *90. Jahrestagung DPG,* O81 (2011)

Danksagung

Für die Überlassung des Themas, intensive Betreuung und Anleitung zum wissenschaftlichen Arbeiten möchte ich mich bei Frau Dr. Veronica Egger bedanken. Herrn Prof.Dr Bernd Sutor möchte ich mein Dank für Möglichkeit aussprechen, diese Arbeit abschließen zu können. Ferner gilt mein Dank der Unterstützung im Labor und im technischen Bereich Frau Irene Schneider und Herrn Robert Waberer.

Für die herausragende Anleitung im Bereich Statistik und für seine Geduld und moralische Erbauung bedanke ich mich bei meinem Mann Sergey Vasenev. Auch bei meiner Mutter Frieda Stroh und bei meinem verstorbenen Vater Andreas Stroh, die durch mein Studium und meine Promotion hindurch mich unterstützt hatten. Und letztlich bei meinem am 02.06.2012 geborenen Sohn Richard, der mich nachts schlafen und am Tag arbeiten ließ.